



1 Ventilation and low pollution enhancing new particle formation in 2 Milan, Italy

3 Myriam Agro¹, Manuel Bettineschi¹, Silvia Melina^{2,a}, Diego Aliaga^{1,b,c}, Andrea Bergomi², Beatrice
4 Biffi³, Alessandro Bigi⁴, Giancarlo Ciarelli¹, Cristina Colombi³, Paola Fermo², Ivan Grigioni², Veli-
5 Matti Kerminen¹, Markku Kulmala¹, Janne Lampilahti¹, Angela Marinoni⁵, Celestine Oliwo^{4,6}, Juha
6 Sulo^{1,d}, Gianluigi Valli⁷, Roberta Vecchi⁷, Tuukka Petäjä¹, Katrianne Lehtipalo^{1,8}, Federico Bianchi¹

7 ¹Institute for Atmospheric and Earth System Research / Physics, Faculty of Science, University of Helsinki, Helsinki, 00014,
8 Finland

9 ²Department of Chemistry, University of Milan, 20133, Milan, Italy

10 ³Air Quality Department, Regional Agency for Environmental Protection of Lombardy, Milan, 20124, Italy

11 ⁴Department of Engineering, University of Modena and Reggio Emilia, Modena, 41125, Italy

12 ⁵Institute of Atmospheric Sciences and Climate, National Research Council of Italy, Bologna, 40129, Italy

13 ⁶Scuola Universitaria Superiore IUSS, 27100, Pavia, Italy

14 ⁷Department of Physics, University of Milan, 20133, Milan, Italy

15 ⁸Atmospheric Composition Research, Finnish Meteorological Institute, Helsinki, 00101, Finland

16 ^anow at: Ecogeo s.r.l., 24122, Bergamo, Italy

17 ^bnow at: Department of Environmental Science, Stockholm University, 11418 Stockholm, Sweden

18 ^cnow at: Bolin Centre for Climate Research, Stockholm University, 11418 Stockholm, Sweden

19 ^dnow at: School of Earth and Atmospheric Sciences, Queensland University of Technology, Brisbane, 4067, Australia

20 *Correspondence to:* Myriam Agro' (myriam.agro@helsinki.fi)

21 **Abstract.** New Particle Formation (NPF) is a crucial process that significantly affects the number of atmospheric particles,
22 forming a substantial portion of the total aerosol population. Therefore, it has important implications for both human health
23 and climate. While extensive research has been conducted in rural areas of the Po Valley, Italy, there is a substantial lack of
24 continuous measurements with state-of-the-art instruments in Milan, one of the most industrialized and densely populated
25 cities in the region. This study aims to address this gap by analysing one year of detailed particle number size distribution
26 measurements between 1.2 and 480 nm at an urban background site in Milan. These data were used to examine the
27 occurrence and characteristics of NPF and to identify how the meteorological and air pollution conditions affect it. We show
28 that a cleaner atmosphere, meaning lower concentrations of air pollutants and lower condensation sink, and a higher
29 ventilation promote NPF. Detailed modelling of the air masses history further revealed that a longer residence time in the Po
30 Valley and a greater exposure to anthropogenic emission sources inhibit NPF. Furthermore, we show that strong winds,
31 particularly from the northwest sector (e.g., Foehn winds), facilitate NPF, likely by reducing the condensation sink for
32 precursor vapours. This locates Milan among the urban sites where atmospheric cleaning enhances NPF, providing insights
33 for urban air quality management.

34



35 1 Introduction

36 New Particle Formation (NPF) is a critical process happening in the atmosphere, consisting of the formation of molecular
37 clusters and their growth through the condensation of precursor vapors (e.g. Kulmala et al., 2013). These newly formed
38 particles play a vital role in influencing air quality (Kulmala et al., 2021). Ultrafine particles (UFP), i.e., particles smaller
39 than 100 nm in diameter, can reach the lungs, blood system, and brain, threatening human health (Schraufnagel, 2020;
40 Vallabani et al., 2023). Moreover, when newly formed particles grow in size, they can interact directly with the solar
41 radiation or be activated as cloud condensation nuclei (Gordon et al., 2017; Merikanto et al., 2009; Spracklen et al., 2008;
42 Zhao et al., 2024), affecting the radiative balance of the Earth and, therefore, the climate. WHO recommended the
43 monitoring of UFP in 2021 (WHO, 2021), and, to comply with such recommendation, the European Union enforces their
44 measurements on the member states with the Ambient Air Quality Directive 2024/2881. European countries must monitor
45 UFP at both urban and rural supersites, as well as in UFP hotspots. Specifically, particle number concentration must be
46 measured for particles larger than 10 nm, with no limitation on the maximum size.

47

48 The Po Valley, in northern Italy, is a region of particular interest for studying NPF due to its unique geographical and
49 environmental characteristics. It is one of the most polluted areas in Europe (EEA, 2019), not only due to the intense and
50 diverse emissions (Kuenen et al., 2022), but also due to its enclosed position between the Alps and the Apennines, which
51 favors the accumulation of air pollutants due to the formation of a shallow boundary layer (Vecchi et al., 2004). Previous
52 research in this area has consistently highlighted the relevance of NPF events. The study by Rodríguez et al. (2005),
53 including data between June 1999 and December 2000, explored the relationship between aerosol size distributions and air
54 quality in Ispra, a rural site in the Northern Po Valley, emphasizing the role of NPF in UFP concentration. Their findings
55 showed a negative correlation between UFP number concentration and aerosol mass, underlining the weakness of traditional
56 air quality metrics, like $PM_{2.5}$ and PM_{10} , which do not effectively capture UFP pollution. According to Rodríguez et al.
57 (2005), NPF events predominantly occurred under clean air conditions, often triggered by Foehn wind coming from the
58 north, which reduced the number of pre-existing particles and created favorable conditions for the new particles to grow. In
59 contrast, polluted conditions promoted the condensation of vapors on pre-existing particles. A study by Hamed et al. (2007)
60 conducted over three years at the rural site of San Pietro Capofiume, Po Valley, found that nucleation events occurred on
61 36% of the days, with the highest frequency in spring and summer (peaking to ~70% in May and July) and the lowest in
62 winter and autumn. Favorable conditions for nucleation included higher temperature, wind speed, solar radiation, and SO_2
63 and O_3 concentrations, while relative humidity and NO_2 levels were lower during event days. The back trajectory analysis
64 indicated that air masses primarily originated from the north and east during nucleation events, highlighting the significant
65 impact of atmospheric circulation on NPF.

66 Supporting the NPF relevance in the area, Kontkanen et al. (2016) reported frequent NPF (86% of days) during a 1-month
67 summer campaign at the same site. Focusing on sub-3 nm clusters, this study indicated high cluster concentrations also



68 during high condensation sink (CS) episodes and non-NPF events, hinting at a continuous formation of the smallest particles.
69 During NPF days, cluster formation peaked with the decrease of CS and relative humidity and the increase in boundary layer
70 height (BLH), highlighting the role of atmospheric dynamics in the process. Sulfuric acid was identified as a potentially
71 relevant precursor to the NPF process. More recent findings by Cai et al. (2024), including direct measurements of the NPF
72 precursor vapors, supported these observations, showing that NPF events occurred on approximately 66% of days during a
73 two-month spring campaign in San Pietro Capofiume, confirming favorable conditions for NPF in this region. During these
74 events, high concentrations of sulfuric acid ($8.5 \cdot 10^6 \text{ cm}^{-3}$) were detected, underlining its crucial role in NPF, alongside
75 ammonia and amines. These studies collectively suggest that NPF substantially contributes to the UFP concentration and
76 overall pollution levels in this area, underscoring its importance for both regional air quality and climate. All the previously
77 cited studies, though, refer to rural areas, while none provide a detailed study of NPF in urban areas of the Po Valley.
78

79 Several factors differentiate rural and urban environments in regard to NPF. The higher CS in urban areas (Bae et al., 2010;
80 Cai et al., 2024) can suppress NPF, as the available precursor vapors tend to condense onto existing particles rather than
81 forming new ones (Seinfeld and Pandis, 2016). The availability, chemical composition, and temporal variation of precursor
82 vapors are also different in rural and urban areas, as they are affected by human activities and local sources, such as traffic.
83 The work by Nieminen et al. (2018), for example, showed that formation rates generally increase with an increasing
84 anthropogenic influence in the atmospheric composition, highlighting the importance of anthropogenic vapors in the NPF
85 process. Urban environments are characterized by various emission sources that release both potential precursor vapors and
86 particles across a wide size range, largely complicating the observation of NPF. In such settings, distinguishing between
87 primary and secondary particles is thus challenging. Therefore, studying NPF in urban areas requires a comprehensive
88 approach that accounts for the complex interplay of various processes, including emissions, atmospheric chemistry, and
89 meteorological conditions. Understanding these interactions is essential for accurately characterizing the NPF mechanism in
90 such environments. Several studies have already been conducted in urban sites across the world, such as the Chinese
91 megacities (Dai et al., 2023; Guo et al., 2014; Yao et al., 2018) and European cities (Brean et al., 2020; Salma et al., 2011),
92 which are discussed in Sect. 3.2. Within this context, the city of Milan provides a particularly complex environment for
93 investigating NPF. As a major metropolitan area within the Po Valley, Milan is characterized by high population density,
94 intense traffic, and significant industrial activities. Its geographical location further aggravates air quality challenges, as
95 atmospheric stagnation often leads to the accumulation of pollutants (Vecchi et al., 2004). This combination of factors makes
96 Milan an important hotspot for studying air quality and the processes driving NPF in urban settings.
97

98 In this study, we present a one-year measurement campaign conducted in an urban background site in Milan between the end
99 of March 2023 and the end of March 2024, as ancillary measurements to the activities foreseen by the European project Ri-
100 Urbans (<https://riurbans.eu>). The main objective was to quantify the intensity, characteristics, and driving mechanisms of
101 NPF. By integrating measurements of particle number size distributions, air pollutant concentrations, and meteorological

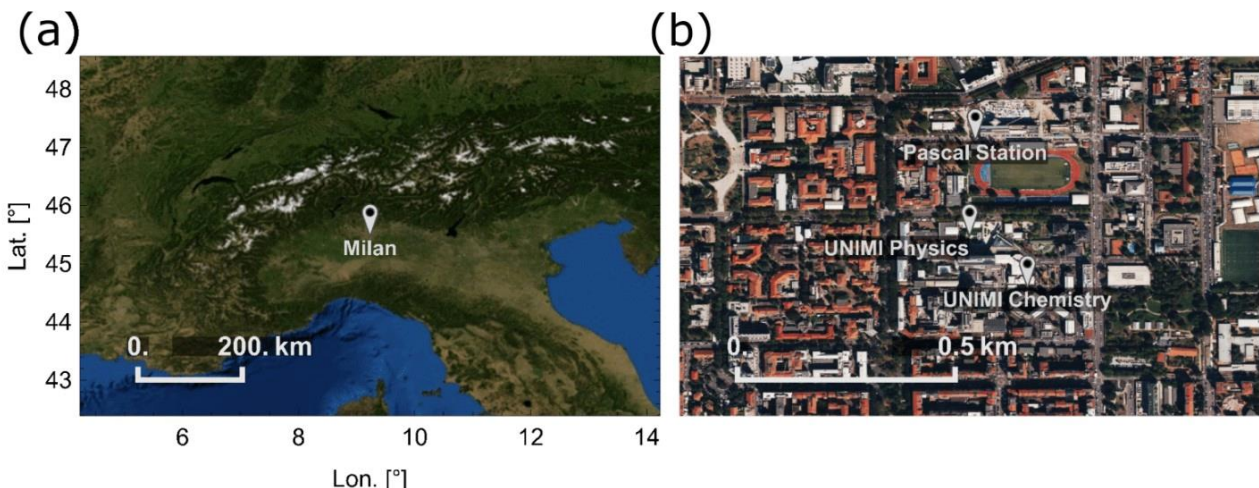


102 conditions, along with outputs from the FLEXible PARTicle dispersion model (FLEXPART), we investigated the key
103 factors governing NPF. By presenting a dataset of particle number size distributions extending down to 1.2 nm, we also
104 evaluated the influence of the 10 nm cut-off diameter of the European air quality directive 2024/2881 on reported particle
105 number concentrations in urban Milan.

106 2 Data and methods

107 2.1 Location description

108 Milan is located in the Po Valley (Fig. 1a) at the coordinates 45.47°N, 9.19°E, at an altitude of 120 m a.s.l. It is the most
109 populated city of the Po Valley with a population of ~1.4 million, reaching ~3.2 million when considering the entire
110 metropolitan area (Istat, 2024). Our measurements were taken in an urban background area, referred to as the Pascal area
111 (Fig. 1b) due to the presence of the Pascal air quality monitoring station of the regional environmental agency (ARPA
112 Lombardia). The area is located in the eastern part of the city of Milan, and the instruments were installed at the Physics
113 (45.4764°N, 9.2317°W) and Chemistry (45.4754°N, 9.2329°W) Departments of the University of Milan (UNIMI). This is an
114 urban background area, which is affected by several sources of pollution, such as traffic, domestic heating, and transported
115 industrial and agricultural emissions (Colombi et al., 2023).



116

117 **Figure 1:** a) Location of the Po Valley and specifically Milan, in white pin. b) Focus on the Pascal area, where the measurement
118 sites (ARPA Lombardia Pascal Station, Physics Department of UNIMI, and Chemistry Department of UNIMI) are located. The
119 satellite maps were generated using Mathematica 14.1 (Wolfram Research, 2025) with imagery from Bing Maps (© Microsoft, last
120 access: April 17th, 2025).



121 2.2 Size distribution data

122 Our size distribution measurements were performed with a set of three instruments: a TSI Scanning Mobility Particle Sizer
123 (SMPS), an Airel Neutral cluster and Air Ion Spectrometer (NAIS), and an Airmodus A11 nano-Condensation Nucleus
124 Counter (nCNC) system, combining an Airmodus A10 Particle Size Magnifier (PSM) and an Airmodus A20 Condensation
125 Particle Counter (CPC). The nCNC and the SMPS were located on the second floor of the Chemistry Department of UNIMI
126 and measured particle number size distributions between 1.2 and 3 nm (Lehtipalo et al., 2022) and 11 and 480 nm,
127 respectively. The NAIS measured number size distributions of particles with a diameter between 2.5 and 40 nm and of
128 positive and negative ions with a diameter between 0.8 and 40 nm (Manninen et al., 2016; Mirme and Mirme, 2013). The
129 instrument was located on the first floor of the Physics Department of UNIMI, at a distance of about 160m from the nCNC
130 and SMPS measurements. The NAIS measurements began in March 2023 and ended in March 2025, while those of the
131 nCNC and the SMPS started in May 2023 and ended in April 2024. The particle number size distribution data between
132 March 27th, 2023, and March 26th, 2024, were used for this study.

133 Considering the high concentration of sub-3nm particles in the city, the nCNC was equipped with an Airmodus Nanoparticle
134 Diluter (AND; Lampimäki et al., 2023) running with a dilution factor of 5 and measuring instrumental background
135 automatically three times a day for 8 minutes. The system was run with a core sampling inlet, as integrated into the AND
136 designed. The nCNC measured in scanning mode with saturator flow scanning between 0.1 l/min and 1.3 l/min. Each scan
137 lasted 4 minutes. To guarantee the correct functioning of the instrument, several checks and cleaning procedures were
138 applied. Every week, both the PSM and the CPC were drained, and their connection was cleaned with isopropanol and
139 compressed air. The involved flows and the background were also manually checked. Flushing of the PSM was performed
140 once every two weeks, while the inlet line was cleaned once a month. The overall status of the instrument was checked
141 almost every day. The data from the nCNC were inverted using the kernel inversion method and applying the corrections for
142 the background, the detection efficiency, the dilution factor, and the inlet losses (Lehtipalo et al., 2022).

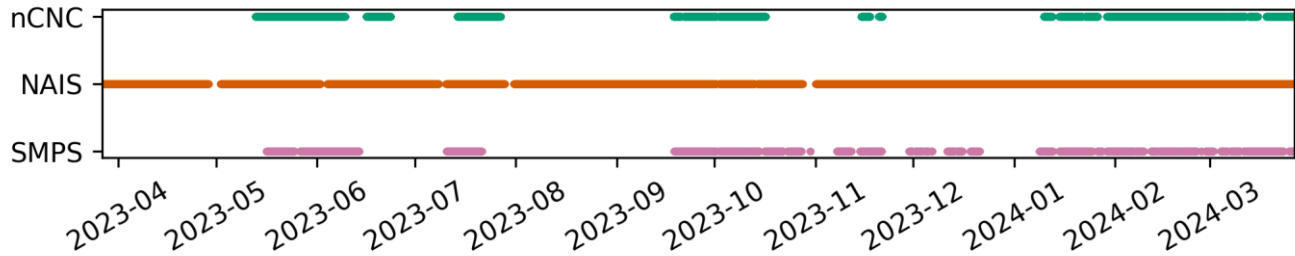
143 The SMPS (Wang and Flagan, 1990), consisting of a 3080 TSI classifier, a 3081 TSI DMA, and a 3772 TSI CPC, was
144 equipped with a 4.9 kV X-ray tube to provide particles with a known charge distribution, and with a silica gel dryer to reduce
145 the relative humidity of the air sample. The DMA scanned between ~10 V and ~ 9700 V during a cycle of 3 minutes,
146 producing size distributions between 11 nm and 480 nm. Weekly checks of the performance of the instrument included CPC
147 draining and flow checks. The inlet line was cleaned once a month with isopropanol and the silica gel was regenerated when
148 needed. The data were inverted using the TSI Aerosol Instrument Manager program. The data were corrected for counting
149 errors due to multiple charging.

150 The NAIS measured in particle, ion, and offset mode, changing mode every 90 seconds. Instrument cleaning was performed
151 when needed. The measured data were inverted automatically by the Spectop software following the procedure described by
152 Mirme and Mirme (2013). The data were then corrected for inlet losses (Gormley and Kennedy, 1948) and ion calibration



153 (Wagner et al., 2016). The final particle number size distributions were obtained by averaging those from the positive and
154 negative columns.

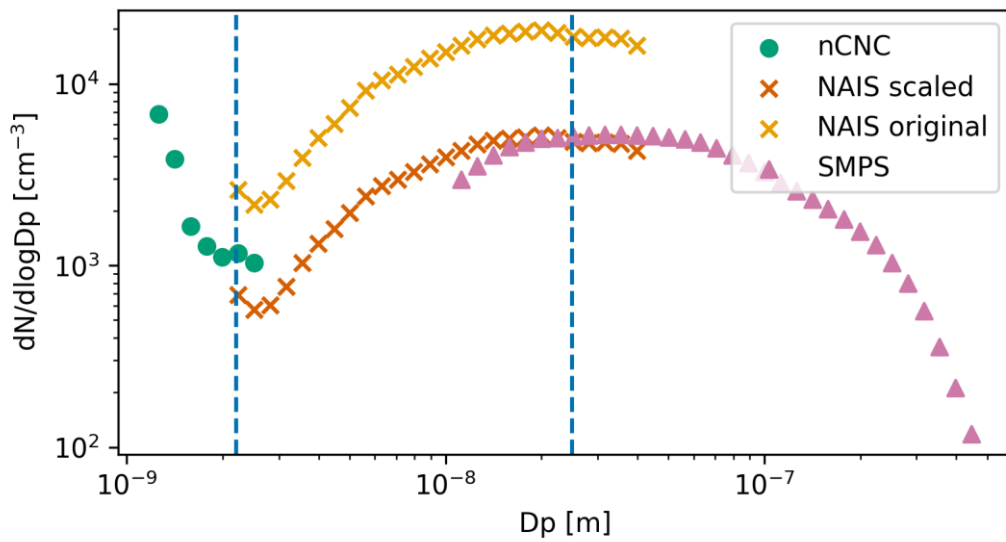
155 Figure 2 illustrates the data availability throughout the campaign. Of all the instruments, the NAIS provided the most
156 comprehensive data coverage, recording data on approximately 97% of the campaign days. On the other hand, the nCNC and
157 SMPS recorded data for about 42% and 45% of the days, respectively. Measurement gaps mostly resulted from technical
158 challenges, including high summer temperatures, power outages, CPC flooding, and delays in equipment shipments.



159

160 **Figure 2: Particle number size distribution data availability throughout the campaign.**

161 The total size distributions were obtained by combining the nCNC, NAIS, and SMPS data. First of all, all the data were
162 resampled to a 15-minute time resolution and rebinned to a diameter resolution of 0.05 in log10 scale. Then, the median size
163 distributions of the three instruments were compared (Fig. 3). A scaling factor of 3.8 was applied to the NAIS data,
164 following the approach proposed by Dada et al. (2023). The scaling factor was obtained by comparing the NAIS and SMPS
165 data in the overlapping size region during the full measurement period. Then, the size distributions of the three instruments
166 were combined at 2.2 nm and 25 nm. Using the SMPS as a reference instrument, an artifact at the connection between the
167 nCNC and the NAIS data was created.



168



169 **Figure 3: Median particle number size distributions measured by nCNC, NAIS (original and scaled), and SMPS. The blue vertical**
170 **lines mark the diameters at which the size distributions were combined.**

171 **2.3 Complementary data**

172 The study included meteorological and air pollutant concentration data provided by ARPA Lombardia, the regional
173 environmental agency responsible for managing multiple monitoring stations across the area. For the analysis, data from the
174 Pascal station, situated approximately 250 m from the UNIMI buildings, were utilized. The meteorological dataset included
175 variables such as atmospheric temperature, wind speed and direction, radiation, and relative humidity. The pollutant
176 concentrations included NO₂, SO₂, O₃, ammonia, and black carbon (BC) concentrations. ARPA Lombardia also provided
177 BLH data for the nearby station of Milano Parco Nord. The BLH was estimated using data from ultrasonic anemometers,
178 applying the Gryning-Batcharova model for convective boundary layer (Batchvarova and Gryning, 1991) and the
179 Zilitinchevich model for stable boundary layer (Zilitinkevich and Baklanov, 2002). All data were recorded with an hourly
180 time resolution.

181 Using these datasets, we calculated the daily Ventilation Index (VI), which reflects the potential of pollutants to disperse
182 efficiently through proper ventilation. For each day, this index is defined as:

183 $VI = \text{mean}(ws) \cdot \text{max}(BLH)$, (1)

184 where ws is the wind speed and BLH is the boundary layer height during that day.

185 In line with ARPA Lombardia guidelines, a VI value of 400 m² s⁻¹ was used as threshold to identify stagnant days.

186 **2.4 Tools and parameters**

187 **2.4.1 Nano-particle ranking**

188 The NPF occurrence was analyzed through the Nano-particle ranking analysis (Aliaga et al., 2023). This method provides an
189 automated, continuous, and objective way of analyzing NPF compared to the manual NPF classification based on the visual
190 inspection of the data and on the identification of a few discrete classes (Maso et al., 2005). The method consists in assessing
191 the intensity and probability of NPF using the change in the concentration of 2.5-5 nm particles during each day. The total
192 concentration of 2.5-5 nm particles from the NAIS, $N_{2.5-5}$, was used to identify the NPF active and background time
193 windows as described by Aliaga et al. (2023), paying particular attention to minimize the impact of traffic rush hours from
194 the active time period, considering that Milan is an urban site. The active region was defined as between 10 and 16 Central
195 European Time (UTC+1), and the background between 23 and 5 Central European Time (UTC+1). The ranking value
196 ($\Delta N_{2.5-5}$) for day i was, then, calculated as follows:

197 $\Delta N_{2.5-5,i} = \text{max}(N_{2.5-5,i_{active}}) - \text{median}(N_{2.5-5,i_{background}})$. (2)

198 The ranking values were then ordered according to their magnitude to determine the percentile rank of each day. The
199 percentile rank of each day indicates the proportion of days with lower $\Delta N_{2.5-5}$ than the value of such day. Therefore, the
200 days with a lower percentile rank have lower $\Delta N_{2.5-5}$, indicating weaker NPF than those with higher percentile rank.



201 2.4.2 Model simulation

202 The Weather Research and Forecasting (WRF) model (v3.71), a regional meteorological model, was employed in this study.
203 The model was driven by the data from the National Centers for Environmental Prediction (NCEP) Climate Forecast System
204 (CFSv2), with a temporal resolution of 6 hours and a horizontal resolution of 1°. For the simulation, the WRF model was
205 configured over a domain with a spatial resolution of $18 \times 18 \text{ km}^2$ (Fig. S1) centered on Milan and roughly covering Europe.
206 WRF simulations were performed using the Rapid Radiative Transfer Model radiation scheme (Mlawer et al., 1997), the
207 Thompson aerosol-aware microphysics scheme (Hong et al., 2004), the Monin–Obukhov surface-layer scheme (Janjic,
208 2003), and the NOAA Land Surface Model scheme (Chen and Dudhia, 2001). The Mellor–Yamada–Janjic turbulent kinetic
209 energy (TKE) scheme (Janjić, 1994) was chosen to assess the boundary layer. WRF simulations were performed on 33
210 vertical sigma layers. Annual anthropogenic emission fluxes for SO_2 and NO_x (see for example, the map of NO_x emissions in
211 Fig. S2) were retrieved from the CAMS datasets at $0.1 \times 0.1^\circ$ (around 10 km) horizontal resolution and distributed hourly
212 over the investigated period, with temporal profiles based on the EMEP MSC-W model (Simpson et al., 2012). The
213 FLEXPART (FLEXible PARTicle dispersion) model, a Lagrangian particle dispersion model, was used to simulate particle
214 transport in the backward direction. In this study, we utilized version 3.3.2 of FLEXPART (Brioude et al., 2013) for
215 backward dispersion to identify the source regions of the air masses reaching Milan. The model was driven by the
216 meteorological data generated from the WRF simulation, with input provided at a temporal resolution of 15 minutes. The
217 FLEXPART domain was aligned with the resolution and extent of the WRF domain. The vertical structure of the domain
218 included 12 levels, spanning from ground level to an altitude of 9000 meters. To conduct the simulation, 10000 particles
219 were released every hour from Milan over the period between April 1st, 2023, and March 31st, 2024. These particles, treated
220 as passive tracers, were emitted from an altitude between 0 to 100 meters above ground level within an $18 \times 18 \text{ km}^2$ area
221 centered on the city. Their trajectories were traced backward in time for up to 72 hours. The backward-mode output from
222 FLEXPART provided the Source-Receptor Relationship (SRR), expressed in units of s, which represents the relative
223 residence time of particles within each grid cell, offering insights into the contribution of specific regions to the air masses
224 arriving in Milan.

225 2.4.3 Condensation sink

226 The Condensation Sink (CS) refers to the rate at which vapors condense onto pre-existing particles in the atmosphere. The
227 CS is influenced by the diffusivity of the condensing molecules, the size distribution of particles, and environmental
228 conditions (Kulmala et al., 2012). It is estimated as:

$$229 CS = 2\pi D \sum_{d'_p} \beta_{m,d'_p} d'_p N_{d'_p}, \quad (3)$$

230 where D is the diffusion coefficient of the condensing vapor in the air (sulfuric acid was assumed), d'_p the particle diameter
231 and $N_{d'_p}$ the concentration of particles with diameter d'_p . β_m was calculated using the Fuchs-Sutugin approximation (Fuchs
232 and Sutugin, 1971). The CS was calculated only when both NAIS and SMPS data were available.



233 2.4.4 Formation rate

234 The formation rate (J) refers to the rate at which new particles appear in a given size range due to nucleation, growth into
235 that size range, or emissions. If the selected size is small enough, it can be assumed that NPF is the main process forming
236 new particles, although the contribution of traffic emissions cannot be excluded in urban environments (Rönkkö et al., 2017).
237 $J_{1.5}$, J_3 , and J_7 were calculated according to the following definition (Kulmala et al., 2012) for the days with a complete size
238 distribution:

$$239 J_{dp} = \frac{dN_{dp}}{dt} + CoagS_{dp}N_{dp} + \frac{GR}{\Delta dp}N_{dp}, \quad (4)$$

240 where $CoagS_{dp}$ is the coagulation sink at size d_p , GR is the growth rate and N_{dp} is the particle number concentration at size
241 d_p . Particle concentrations in the 1.5–3 nm, 3–7 nm, and 7–20 nm size ranges were used to calculate $J_{1.5}$, J_3 , and J_7 ,
242 respectively.

243 The coagulation sink is the rate at which particles are lost due to coagulation with pre-existing particles (Kulmala et al.,
244 2012).

$$245 CoagS_{dp} = \sum_{d'_p=d_p}^{d'_p=d_{pmax}} K(d_p, d'_p)N_{d'_p}, \quad (5)$$

246 where $K(d_p, d'_p)$ is the coagulation coefficient between particles of diameter d_p and d'_p .

247 The Growth Rate (GR) indicates the rate at which particles increase in size over time. Considering the limited variability of
248 the GR values (Kulmala et al., 2022), the median size distribution of the days above the 80th percentile rank was used to
249 calculate the average GR in the size ranges of 3–7 nm, 7–20 nm, and 20–100 nm with the maximum concentration method
250 (Kulmala et al., 2012) to evaluate $J_{1.5}$, J_3 and J_7 respectively (Kerminen et al., 2018). The GR values were calculated using a
251 size interval around the upper limit of the one used for the J calculation, in order to estimate the growth out of the size bin.

252 2.4.5 Sulfuric acid proxy calculation

253 A proxy for sulfuric acid was calculated using the approach described by Dada et al. (2020). The equation for the
254 concentration of sulfuric acid in an urban site was used (Dada et al., 2020).

$$255 [H_2SO_4] = -\frac{CS}{2 \cdot (9.9 \cdot 10^{-9})} + \left[\left(\frac{CS}{2 \cdot (9.9 \cdot 10^{-9})} \right)^2 + \frac{[SO_2]}{9.9 \cdot 10^{-9}} (1.6 \cdot 10^{-9} \cdot GlobRad) \right]^{1/2}, \quad (6)$$

256 where $[SO_2]$ is the SO_2 concentration, $GlobRad$ is the global radiation and CS is the condensation sink.

257 2.4.6 Air mass exposure

258 To investigate the impact of the air masses on NPF, we adapted the Air Mass Exposure (AME) methodology originally
259 proposed by Hakala et al. (2022). In their method, AME calculations combined FLEXPART output with static two-
260 dimensional fields to identify when air masses were exposed to different pollutant emissions.



261 In this study, we modified the AME calculation by incorporating FLEXPART output with dynamic, three-dimensional
262 emissions data from the CHIMERE model, including its temporal variations. For each particle release event, we computed
263 the AME for a specific pollutant or substance x (denoted as AME_x) using emission data for that substance derived from the
264 emission model (emiSURF) output. This approach allowed us to account for the temporal variability of emissions within air
265 masses, enabling a more precise evaluation of the exposure of air masses to pollutant emissions.

266 Given a domain Ω , containing time (t), height (h), longitude (x) and latitude (y) as coordinates, and a release time (τ), the
267 AME_x for a specific τ is calculated according to the following equation:

268
$$AME_x(\tau) = \sum_{(t,x,y) \in \Omega} \sum_{h=0}^{500m} SRR(t, x, h, y; \tau) \cdot X(t, x, y). \quad (7)$$

269 2.4.7 Air mass trajectories description

270 To clearly visualize the origin of air masses, the trajectory density was defined as the absolute difference between the
271 percentage of trajectories passing over each grid cell, regardless of their height, and arriving in Milan on days with a rank
272 above the 80th percentile, and the percentage of all trajectories passing over the same area:

273
$$\Delta\%T = \%T_{>80} - \%T_{tot}. \quad (8)$$

274 Specifically,

275
$$\%T_{>80}(x, y) = \frac{\sum_{\tau \in T_{80}} \delta(\tau; x, y)}{N_{80}}, \quad (9)$$

276

277
$$\%T_{tot}(x, y) = \frac{\sum_{\tau \in \Omega} \delta(\tau; x, y)}{N_{tot}}, \quad (10)$$

278 where T_{80} is the set of releases arriving when the ranking percentile is larger than 80, N_{80} is the total number of these
279 releases, N_{tot} is the total number of releases and, $\delta(\tau; x, y)$ assumes 1 or 0 values as follows:

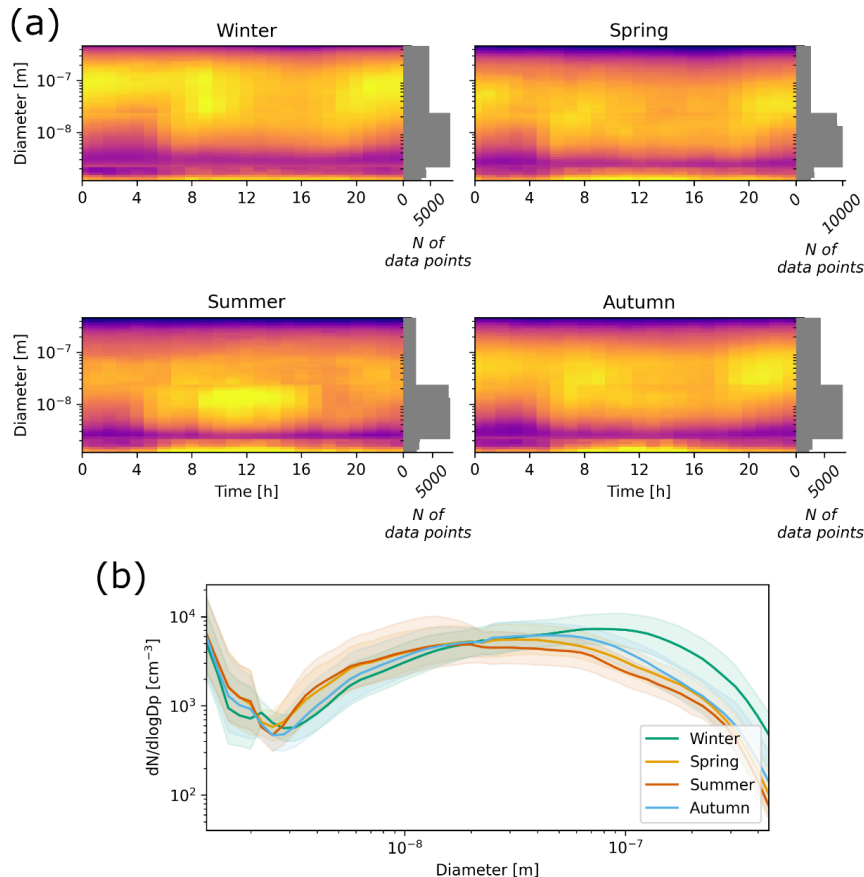
280
$$\delta(\tau; x, y) = \begin{cases} 1 & \text{if } \sum_{(t,h) \in \Omega} SRR(t, h; x, y, \tau) > 0 \\ 0 & \text{otherwise} \end{cases}. \quad (11)$$

281 This means that $\delta(\tau; x, y) = 1$ if, for a given release, at least one of the 10000 released particles passed through the point
282 (x, y) during the previous 72 hours.

283 3 Results and discussion

284 3.1 Size distributions characterization

285 The particle number size distributions in Milan exhibited a clear seasonal cycle, which is illustrated in Fig. 4a and Fig. 4b
286 through the daily average size distribution surface plot per season and the average size distribution per season, respectively.
287 The months of December, January, and February were included in winter; March, April, and May in spring; June, July, and
288 August in summer; September, October, and November in autumn.



289

290 **Figure 4: a) Daily median particle number size distribution surface plot per season. The grey bar plots represent the number of**
291 **data points available for each diameter. Times are in Central European Time, UTC+1. b) Median particle number size**
292 **distribution per season. The shaded areas represent the interquartile ranges.**

293 During winter, the highest concentrations of particles larger than 50 nm were observed (Fig. 4b). This increase was probably
294 the result of both a decrease in the BLH and an increase in biomass burning emissions (Colombi et al., 2023). Moreover, the
295 typical traffic-related pattern was evident, with marked increases across all particle size ranges starting from 5:00 and 17:00
296 Central European Time, UTC+1 (Fig. 4a), coinciding with the morning and evening rush hours.

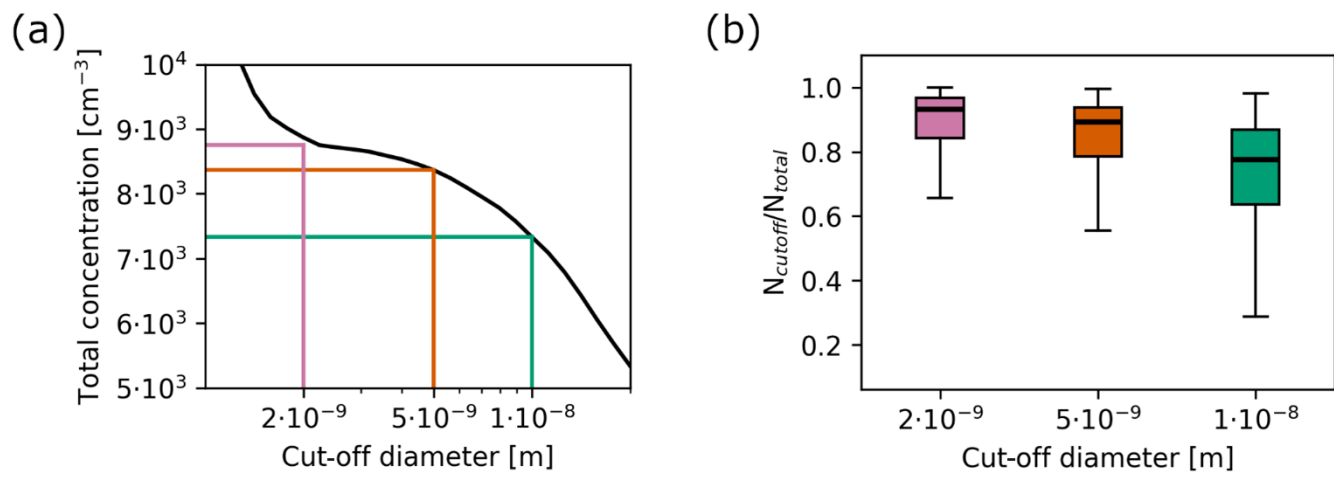
297 In spring, and particularly in summer, these traffic-related peaks became less pronounced, suggesting an increase in the
298 atmospheric mixing. Additionally, the data revealed a clear midday increase in sub-10 nm particles (Fig. 4a), which was
299 most likely associated with NPF events. This phenomenon, which became more pronounced in the warmer months, was
300 driven by photochemical reactions enhanced by higher solar radiation and it was, therefore, mostly observed during spring
301 and summer. During summer, we observed the most significant increase in sub-10 nm particle concentrations, alongside the
302 lowest levels of particles larger than 100 nm (Fig. 4b).



303 In autumn, the traffic-related peaks reappeared (Fig. 4a) due to the combined effect of the increase in traffic emissions
304 (Colombi et al., 2023) and the decrease in atmospheric dispersion and BLH, becoming again a more dominant factor
305 influencing particle concentrations. However, the median concentrations across all particle sizes during autumn remained
306 similar to those observed in spring, indicating a seasonal transition towards winter. Overall, though, considering the
307 discontinuities in the data collection (Fig. 2) and the definition of each season, these conclusions may not be representative
308 of each entire season and their comparison has intrinsic uncertainties.

309 The shape and values of the median size distributions in Fig. 4b are in agreement with those of other urban background sites
310 of southern, central, and eastern Europe (Trechera et al., 2023). The comparison between the characteristics of the size
311 distribution surface plots per season (Fig. 4a) in Milan and other urban background sites (Trechera et al., 2023) also does not
312 point out any anomaly. As observed in Milan, several other urban background sites across Europe showed a more
313 pronounced increase in sub-25 nm particles at midday during the warmer months. Higher concentrations in the same size
314 range due to traffic rush hours were also reported in all urban background sites (Trechera et al., 2023).

315 Considering that we measured size distributions ranging from 1.2 nm to 480 nm, it is relevant to evaluate the implications of
316 the 10 nm cut-off established by the European Union for the measurement of UFP. In Fig. 5, the total particle number
317 concentration at different cut-off sizes was calculated by integrating the size distribution from different lower limits (2 nm, 5
318 nm, and 10 nm) to the upper limit of 480 nm. While the availability and complexity of the instrumentation pose significant
319 challenges to measuring sub-10 nm particles, it is important to explore how much the total concentration is underestimated
320 due to the chosen cut-off size (Fig. 5a). For instance, in our dataset, lowering the threshold from 10 nm to 5 nm would result
321 in an average increase of 14%, whereas adopting a 2 nm cut-off would lead to a 19% increase. Fig. 5b shows the variability
322 of the ratio between the concentration for a certain cut-off size (2, 5, 10 nm) and the total particle concentration. These
323 considerations highlight the potential impact of measurement thresholds on reported UFP concentrations and emphasize the
324 need for further discussion on optimal cut-off values and for improvements in sub-10 nm size distribution measurements.

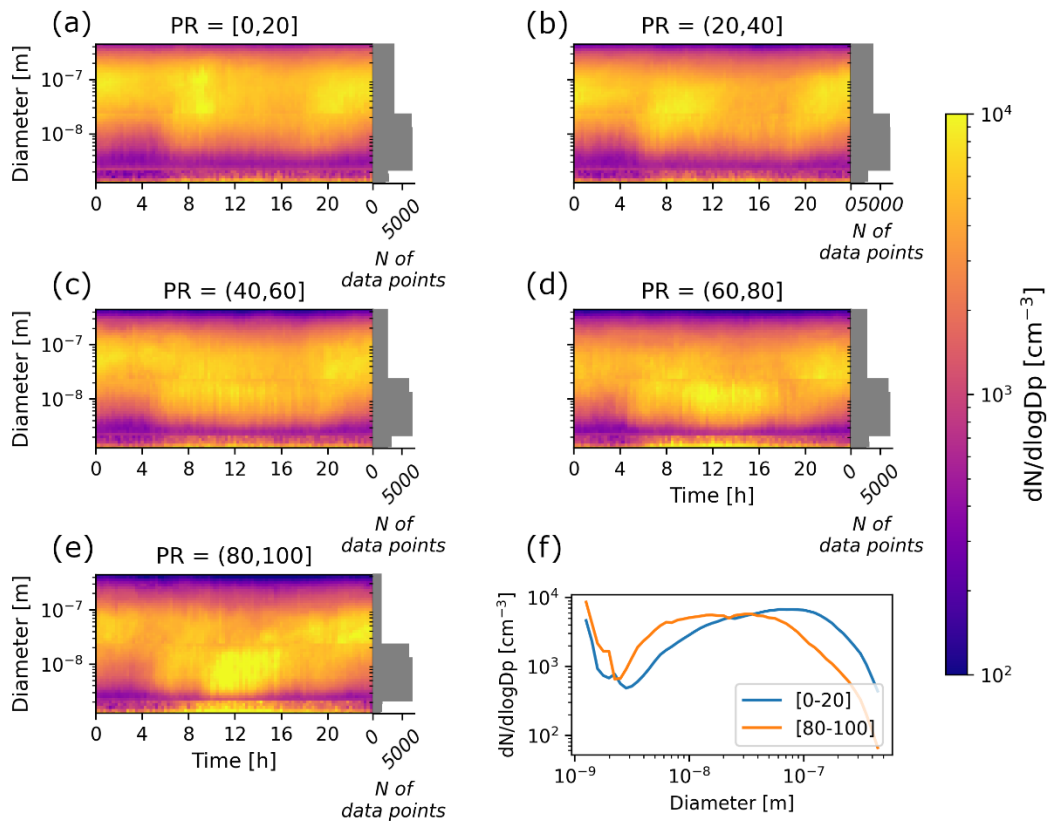




326
327
328
329
330
331 **Figure 5: a) Total particle number concentration at different cut-off sizes, averaged over the whole campaign time. The green line**
332 **represents the cut-off diameter of 10 nm, the orange one of 5 nm, and the pink one of 2 nm. b) Box plots representing the ratio**
333 **between the concentration at different cut-off diameters ($N_{\text{cut-off}}$) and the total particle concentration (N_{total}). The box plots display**
334 **the interquartile range, between the 25th and the 75th percentile, and the median (50th percentile) as a horizontal line inside the box.**
335 **The whiskers of the box plot extend from the edges of the box to the smallest and largest values within 1.5 times the interquartile**
336 **range. Outliers are not shown in this figure.**

332 3.2 NPF analysis

333 The Nano-particle ranking analysis was applied to characterize NPF. At higher percentile ranks, a midday increase in particle
334 concentration across all size ranges became clear, indicating NPF (Fig. 6). The process was marked by an initial rise in 1.2
335 nm particle concentration, followed by an increase in the concentration of larger particles. This pattern indicates that NPF
336 occurred over a wide area, including Milan itself. At lower percentile ranks, higher concentrations associated with traffic
337 rush hours were evident, but they gradually faded at higher percentile ranks (Fig. 6, panels a to e). This pattern aligned with
338 the seasonal variations in particle size distributions and NPF (Fig. S3, Fig. 4a). In fact, lower ranking values $\Delta N_{2.5-5}$,
339 corresponding to weaker NPF, were more frequent during winter (December to February, Fig. S3), when traffic peaks were
340 also more evident (Fig. 4a). Conversely, the strongest NPF events were observed in April and mid-to-high rank values
341 $\Delta N_{2.5-5}$ days (percentile ranks between 60 and 80) occurred predominantly between June and August (Fig. S3), when
342 stronger atmospheric dispersion minimizes the concentration of traffic-related peaks (Fig. 4a).

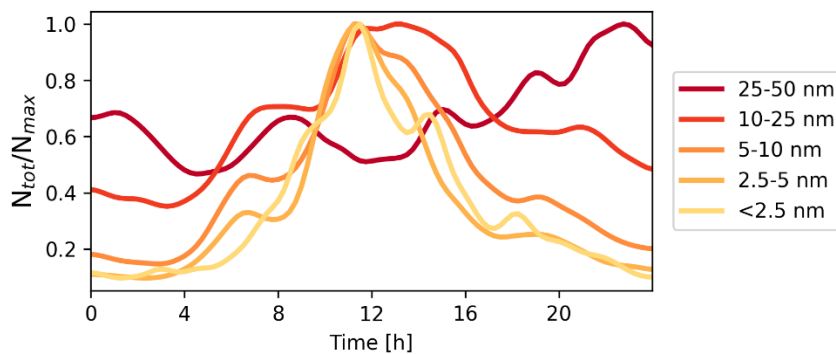


343



344 **Figure 6: Daily median particle number size distribution surface plots, grouped by 20-percentile intervals of NPF rank (PR)**
345 (panels a-e). Times are in Central European Time, UTC+1. Median size distributions < 20 percentile of NPF rank days and > 80
346 percentile of NPF rank days (panel f).

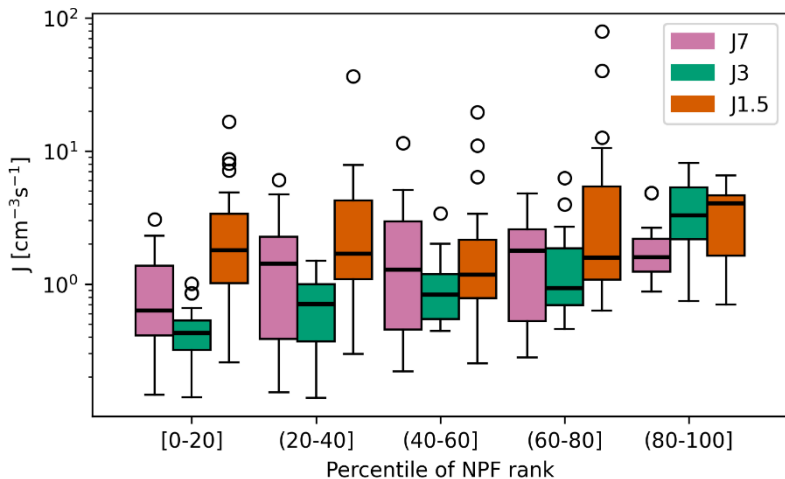
347 Our analysis demonstrates that NPF significantly contributed to the UFP concentration through a growth process that lasted
348 for several hours. As shown in Fig. 7, the concentration of sub-2.5 nm particles increased first, followed sequentially by that
349 of 2.5–5 nm, 5–10 nm, and 10–25 nm particles, reflecting a well-defined growth pattern in increasing size order. Accurately
350 distinguishing the contribution of NPF from that of primary emissions is crucial for a proper interpretation of these patterns.



351
352 **Figure 7: The lines represent the median total concentration of particles within different size bins (<2.5, 2.5-5, 5-10, 10-25, 25-50**
353 **nm), calculated including the days above the 80th percentile of rank. Each line is normalized to its own maximum value and**
354 **smoothed through a Gaussian filter.**

355 GR were calculated as described in Sect. 2.4.4. The values of 1.8 nm h^{-1} , 2.9 nm h^{-1} and 9.7 nm h^{-1} were found for the GR in
356 the size ranges of 3–7 nm, 7–20 nm and 20–100 nm, respectively.

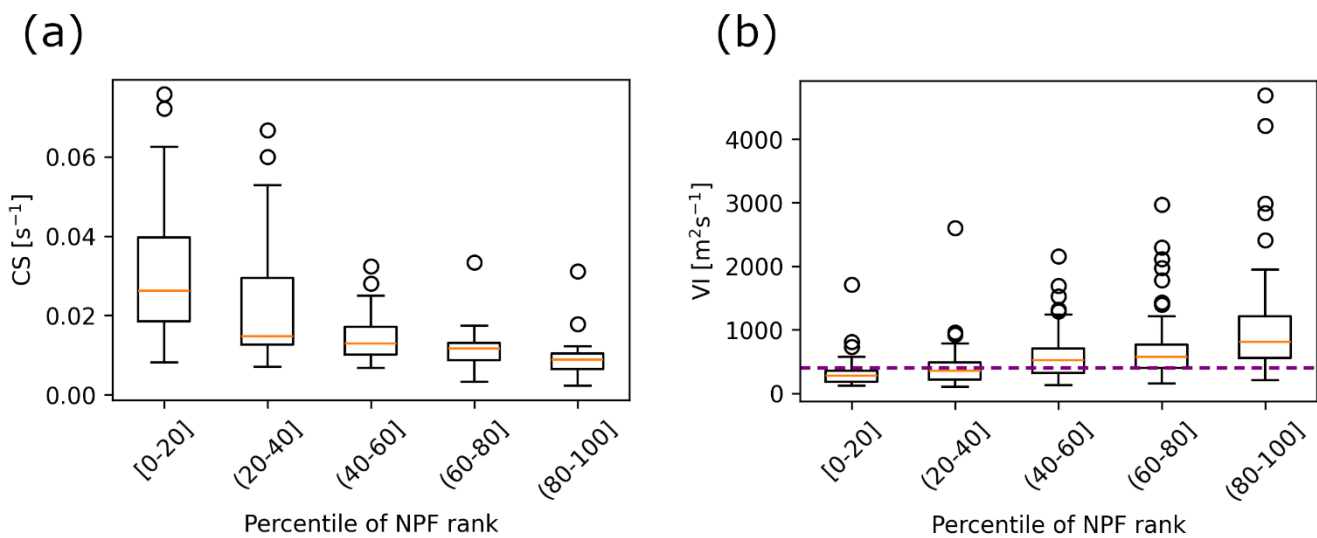
357 The formation rates $J_{1.5}$, J_3 , and J_7 are presented in Fig. 8. While J_3 correlated with percentile ranks — indicating higher
358 production of 3 nm particles (higher J_3) during stronger NPF days (higher ranking) — $J_{1.5}$ remained relatively constant
359 across most ranks. This suggests that clustering, which formed 1.5 nm particles, occurred at the site, but only under certain
360 conditions the particle growth was observed (Kulmala et al., 2013). $J_{1.5}$ reached higher values only in the 80–100 rank bin,
361 suggesting that clustering was more efficient during strong NPF days. Lastly, J_7 did not show a clear increasing trend and
362 was often higher than J_3 , likely due to the influence of traffic in this size range. This is supported by Fig. 4a, where morning
363 traffic peaks are clearly visible in the 5–10 nm size range. The ratio between J_7 and J_3 suggests that, for days with rank
364 below the 80th percentile, traffic was a stronger source of particles larger than 7 nm than NPF. During high-rank days (80th –
365 100th percentile), when NPF events were stronger, a marked increase in J_7 would have been expected as result of a dominant
366 contribution from NPF. However, such an increase was not clearly observed, implying that traffic may have remained the
367 dominant contributor to particles larger than 7 nm even during the most intense NPF days.



368

369 **Figure 8: Maximum $J_{1.5}$, J_3 , and J_7 during the active window, per rank class. For the box plot description, refer to Fig. 5b.**

370 The Nano-particle ranking method allows a continuous analysis of the NPF process in relation to meteorological and
371 dispersion variables and pollutant concentrations. To understand which parameters affected the process, the atmospheric
372 conditions within each bin of 20-percentile rank were compared. Figure 9 illustrates the relationships of CS and ventilation
373 index VI, defined in Eq. (1), with rank as an example. Higher CS corresponded to low-rank days, while a high VI
374 corresponded to high-rank days. Black carbon, NO_2 , SO_2 , PM_{10} , and $PM_{2.5}$ concentrations reported the same trend as CS,
375 while BLH behaved as the ventilation index (Fig. S4, S5, and S6). Therefore, it is clear that cleaner air conditions and
376 stronger atmospheric mixing correlated with enhanced NPF. In particular, intermediate-strong NPF (percentile rank > 60%)
377 happened, on average, only during non-stagnant days and low CS ($< 0.007 s^{-1}$ on average).



378



379 **Figure 9: a) Median CS calculated over the active time window of each day and b) daily ventilation index (VI) per rank class. The**
380 **purple dotted line represents the threshold of VI=400 m²s⁻¹ for stagnant days. For the explanation of box plots, refer to Fig. 5b.**

381 Our data allowed a comparison between the environmental conditions and NPF in Milan and other urban locations. In Milan,
382 the CS varied between 0.01 s^{-1} (during strong NPF events, Fig. 9a) and 0.03 s^{-1} (during weak NPF events, Fig. 9a), which is
383 comparable to the values observed in Shanghai (CS between 0.01 s^{-1} and 0.02 s^{-1} on average; Yao et al., 2018). However,
384 while the particle formation rate at 1.5 nm ($J_{1.5}$) in Milan remained below $10^2\text{ cm}^{-3}\text{s}^{-1}$ (averaging around $10^1\text{ cm}^{-3}\text{s}^{-1}$), it
385 reached up to $10^3\text{ cm}^{-3}\text{s}^{-1}$ in Shanghai (Yao et al., 2018). This is likely due to differences in the precursor vapor
386 concentrations and atmospheric conditions. However, without precursor vapor measurements in Milan, this hypothesis
387 remains uncertain.

388 GR also differed between the two cities. In Shanghai, the GR was approximately 6 nm h^{-1} for $3\text{--}7\text{ nm}$ particles and 9 nm h^{-1}
389 for $7\text{--}25\text{ nm}$ particles (Yao et al., 2018), whereas in Milan, the values were significantly lower, specifically, 1.8 nm h^{-1} and
390 2.9 nm h^{-1} for $3\text{--}7\text{ nm}$ and $7\text{--}20\text{ nm}$ particles, respectively. A similar relation is observed in Nanjing, where both recorded
391 GR and J were higher than in Milan. For example, the average J_3 in Nanjing ranged between $7.4\text{ cm}^{-3}\text{s}^{-1}$ and $13.9\text{ cm}^{-3}\text{s}^{-1}$,
392 while the GR of 10 nm particles was between 13.4 nm h^{-1} and 14.5 nm h^{-1} , depending on the type of event (Dai et al., 2023).

393 NPF has also been extensively studied in European cities. In Barcelona, for instance, Brean et al. (2020) reported an average
394 GR of 4.69 nm h^{-1} and 4.36 nm h^{-1} for 4.5 and 1.9 nm particles, respectively. The CS in Barcelona was lower during NPF
395 event days compared to non-event days, but it remained below 0.02 s^{-1} in both cases, slightly lower than the values recorded
396 in Milan. When comparing formation rates, Milan exhibited weaker NPF. While $J_{1.9}$ in Barcelona frequently fell between $10\text{ cm}^{-3}\text{s}^{-1}$ and $10^3\text{ cm}^{-3}\text{s}^{-1}$ (Brean et al., 2020), $J_{1.5}$ in Milan was mostly limited to the range of $1\text{ cm}^{-3}\text{s}^{-1}$ to $10\text{ cm}^{-3}\text{s}^{-1}$, indicating
397 a lower particle formation intensity. In Budapest, the GR of 6 nm particles was 7.7 nm h^{-1} on average, while J_6 was $4.2\text{ cm}^{-3}\text{s}^{-1}$,
398 higher than what was observed in Milan in both cases. The CS in Budapest was lower than in Milan during non-event days
399 but in line with Milan values during NPF event days (Salma et al., 2011). Finally, the study by Bousiotis et al. (2021)
400 compared size distributions and NPF characteristics in several urban sites across Europe (Denmark, Germany, Spain,
401 Finland, and Greece), distinguishing urban background and roadside sites. Reported J_{10} were higher in roadside sites, but
402 overall lower than what was observed in Milan. On average, they remained below $0.1\text{ cm}^{-3}\text{s}^{-1}$ in all sites, except for German
403 roadside sites, where the average J_{10} was higher but still below $0.2\text{ cm}^{-3}\text{s}^{-1}$. The reasons for these differences may partially
404 reside in the differences across sites, but they are not clear. GR for 10 nm particles was, on average, between 2 nm h^{-1} and 5 nm h^{-1} , in line with the value found in Milan for that of 7 nm particles (2.9 nm h^{-1}).

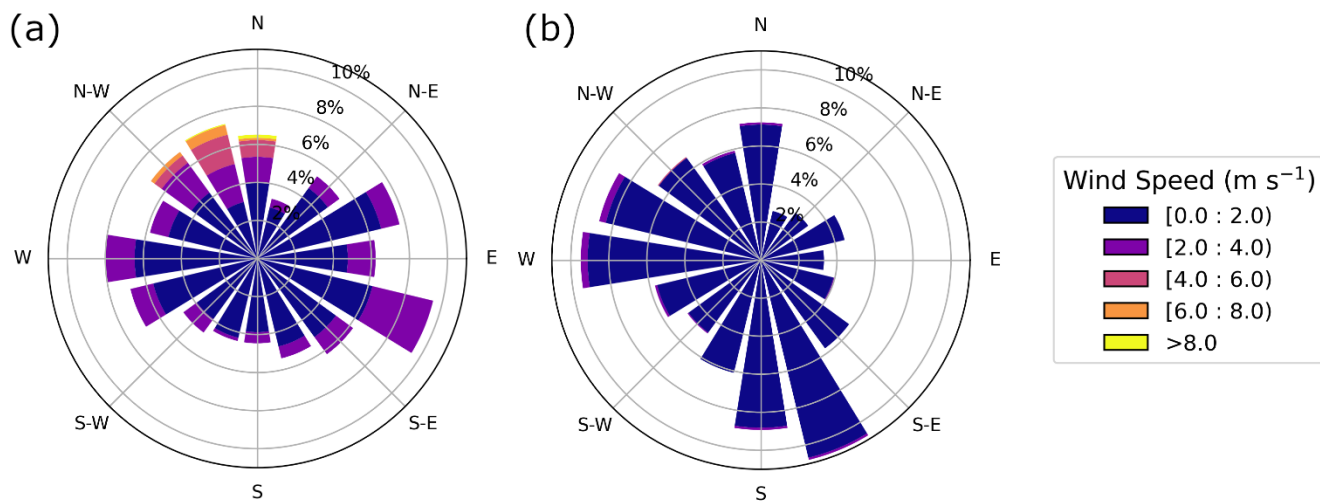
405 If we compare our results to previous studies in the rural areas of the Po Valley, it is clear that lower $J_{1.5}$ were observed in
406 Milan. Cai et al. (2024) observed an average $J_{1.7}$ of $10^2\text{ cm}^{-3}\text{s}^{-1}$ in San Pietro Capofiume during NPF days, which was
407 significantly higher than what was found in Milano ($J_{1.5}$ was about $3\text{ cm}^{-3}\text{s}^{-1}$). However, the values for J_3 and J_7 were more
408 similar. GR were also higher than in Milan (around 4 nm h^{-1} for $3\text{--}7\text{ nm}$ particles and around 5 nm h^{-1} for $7\text{--}15\text{ nm}$ particles).
409 The recorded CS was below 0.01 s^{-1} during both NPF and non-NPF and therefore lower than in Milan, where NPF is
410 possibly suppressed more than in the rural areas.



413 When comparing all the results, though, it is critical to take into consideration the possible differences in the methodologies
414 for estimating the formation and growth rates, including the slightly different size ranges used in different studies, which
415 contribute to the uncertainty in the comparisons.

416 **3.3 Air mass modelling analysis in relation to NPF**

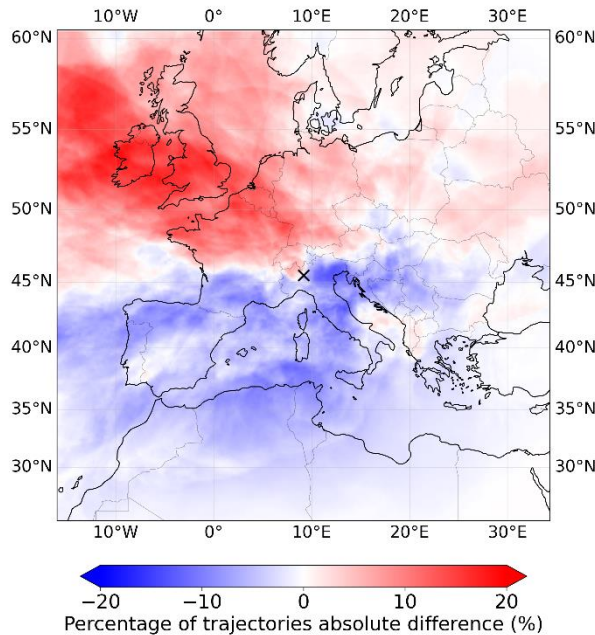
417 The analysis of NPF in relation to the meteorological conditions at the site pointed out that strong wind from northwest was
418 a favorable condition for NPF at this site (Fig. 10).



419

420 **Figure 10: Wind rose for a) strong NPF days (percentile rank > 80) and for b) weak NPF days (percentile rank < 20).**

421 In order to explore further such relation and the characteristics of the air masses that favor the formation of new particles, the
422 Lagrangian particle dispersion model FLEXPART, driven by the meteorological output from WRF simulations, was applied
423 to identify the eventual preferential air mass direction for NPF and its characteristics.

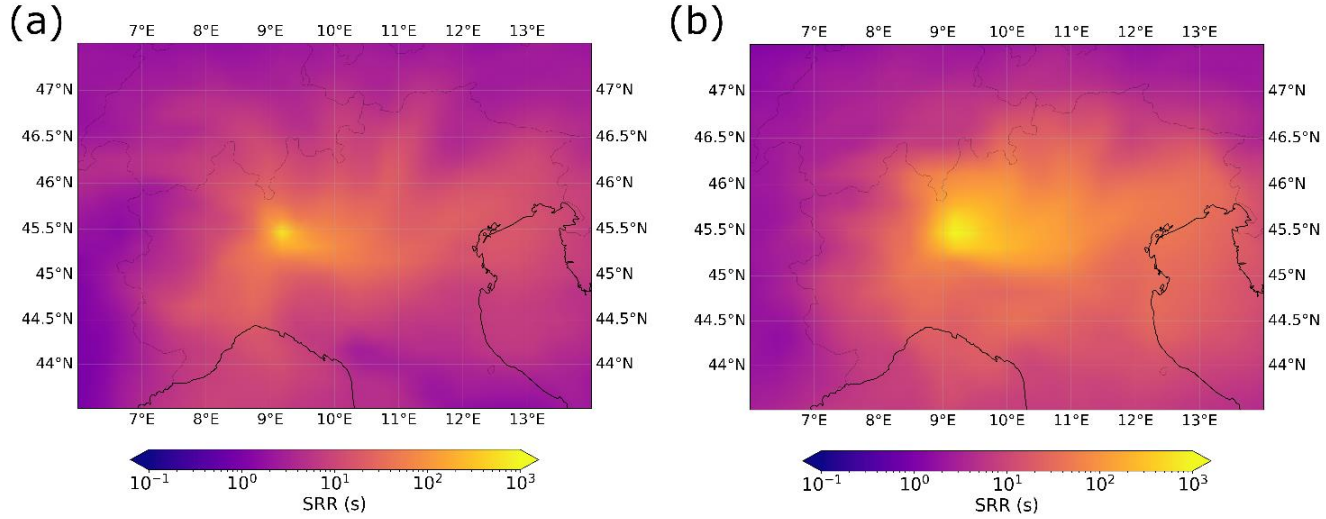


424

425 **Figure 11:** Air masses reaching the measurement site. The color scale represents the difference between the percentage of
426 trajectories passing over a given area and reaching Milan during a day with a rank > 80 and the percentage of the total
427 trajectories passing over a given area. The details of the metric are reported in Sect. 2.4.7. An X marks the location of Milan on the
428 map.

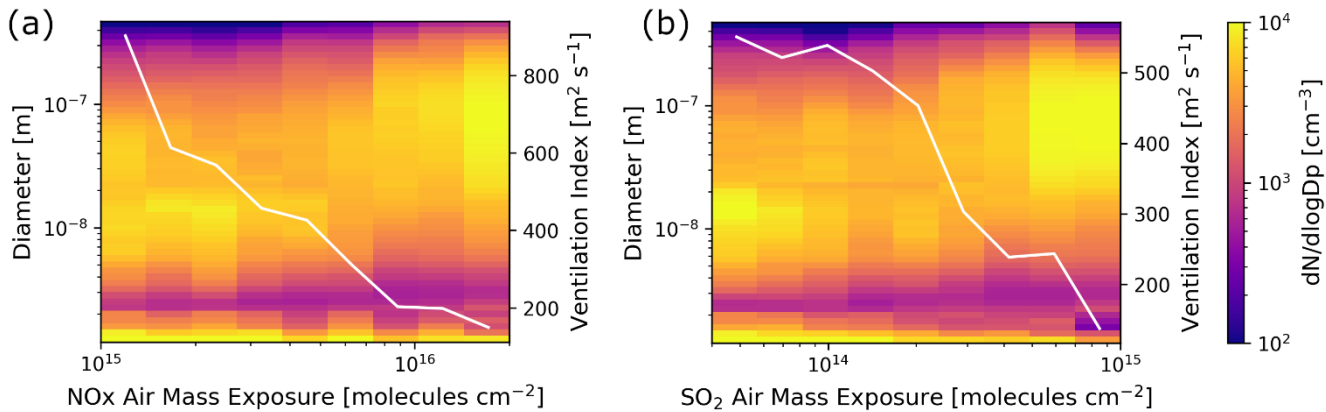
429 The air mass trajectory density, calculated as described in Eq. (8), emphasizes that north, particularly northwest, was the
430 preferred direction for NPF (Fig. 11). An east-west axis distinctly separated the north and south sectors: air masses arriving
431 in Milan from the north promoted NPF, while those from the south hindered it.

432 Focusing on the Po Valley only (Fig. 12), it is clear that a lower air mass residence time in the area produced stronger NPF.
433 This agrees with both the anticorrelation between NPF rank and wind speed and with the anticorrelation between NPF rank
434 and pollutant concentrations, as the Po Valley is rich in emission sources. Lower exposure to anthropogenic sources
435 enhanced NPF in this location, as shown in Fig. 13. Lower air mass exposure to NO_x and SO_2 sources was associated with
436 higher concentration of small (sub-2.5 nm) particles, to a broader cluster band, extending to 2.5 nm, and to a smaller
437 accumulation mode. On the other hand, at higher NO_x and SO_2 air mass exposure, the cluster particles remained smaller (up
438 to ~ 1.5 nm) and had lower concentrations. Furthermore, the accumulation mode reached larger sizes. Overall, these
439 observations indicate that lower air mass exposure to anthropogenic sources favored the formation of new particles. The air
440 mass exposure to both NO_x and SO_2 sources correlated with the median ventilation index, which decreased at increasing air
441 mass exposure, supporting the role of atmospheric ventilation (Fig. 13).



442

443 **Figure 12: Source-Receptor Relationship (SRR) below 500 m during a) strong NPF days (percentile rank > 80) and during b) weak**
444 **NPF days (percentile rank < 20).**



445

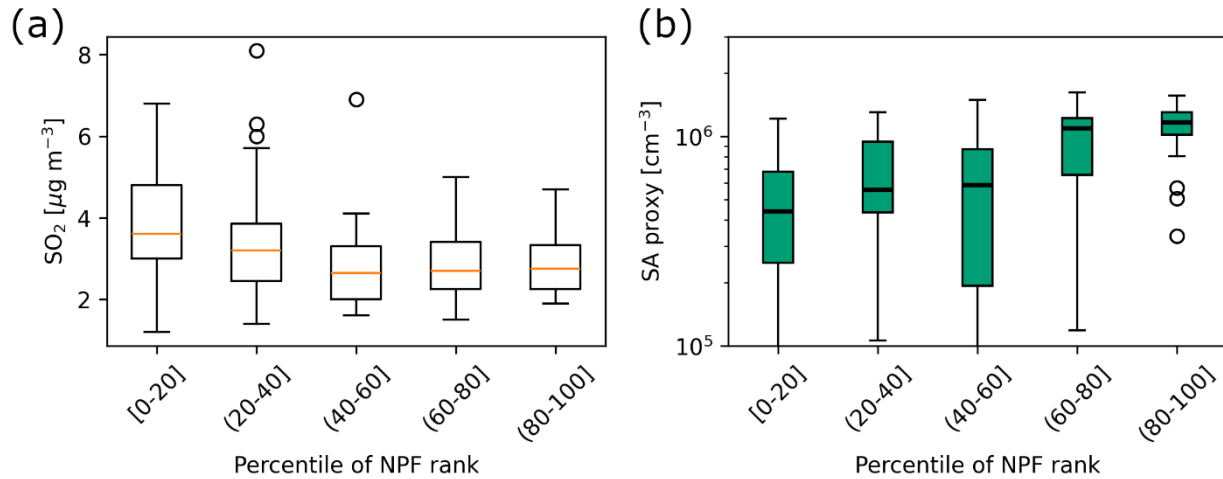
446 **Figure 13: Relationship between a) Air Mass Exposure to NOx emissions and particle number size distribution and b) Air Mass**
447 **Exposure to SO₂ emissions and particle number size distribution. The white lines represent the median Ventilation Index.**

448 3.4 Sulfuric acid proxy analysis

449 The role of sulfuric acid, which has been identified in previous studies as a critical precursor vapor in the Po Valley (Cai et
450 al., 2024), was investigated through its proxy, calculated as described in Sect. 2.4.5. The sulfuric acid proxy showed an
451 increasing trend with percentile ranks (Fig. 14b), indicating its contribution to the NPF process. However, SO₂, a precursor



452 for sulfuric acid, showed the opposite trend (Fig. 14a), similar to that of CS and of other pollutants (BC, PM₁₀, PM_{2.5}, NO₂).
453 This hints at the role of high CS in inhibiting NPF.



454

455 **Figure 14: a) SO₂ daily median concentration calculated over the active time window and b) sulfuric acid (SA) proxy daily median**
456 **calculated over the active time window per rank class. For the description of the box plots, refer to Fig. 5b.**

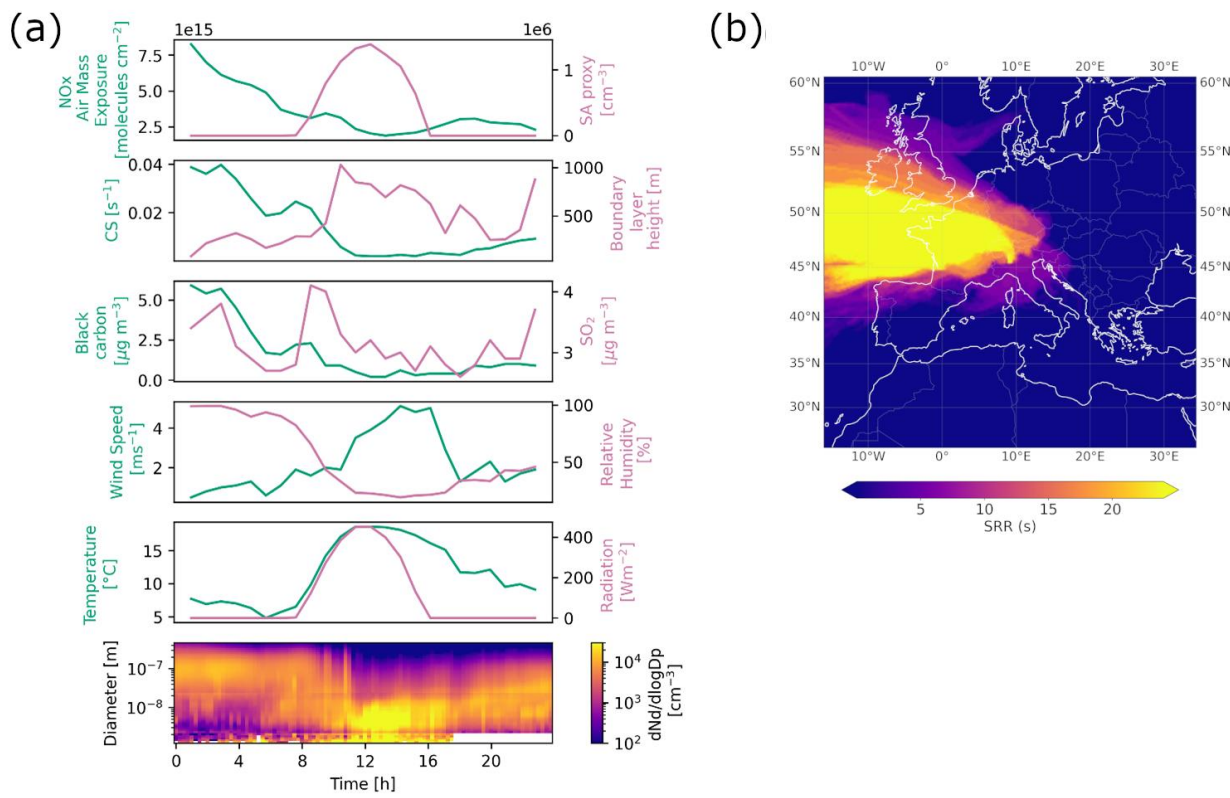
457 3.5 Case study

458 In this section, we present an example of NPF day, featuring the characteristics discussed so far (lower CS and BC
459 concentration, higher BLH, and lower exposure to anthropogenic emissions). Specifically, we focus on November 17th,
460 2023, a day that fell within the 80-100 class of percentile rank (Fig. 15). On this day, local clustering led to an increase in the
461 concentration of sub-3 nm particles starting at 8 am (UTC+1), followed by a subsequent rise in the concentration of particles
462 up to 100 nm in diameter (Fig. 15a), indicating condensational growth. These phenomena were observed in correspondence
463 with a decrease in CS, in BC concentration, and in air mass exposure to NO_x sources, as well as an increase in wind speed
464 and BLH (Fig. 15a), suggesting strong atmospheric mixing. Additionally, the air mass trajectory analysis revealed a
465 dominant flow from northwest (Fig. 15b). Oppositely to the average results that have been shown so far, SO₂ concentration
466 showed a sharp increase as the event began.

467 On this day, the phenomenon driving the free tropospheric air masses advection and atmospheric clearing was the Foehn
468 wind — a warm, dry wind descending from the Alps — which brings clear skies and higher temperatures compared to
469 seasonal averages, together with exceptionally low pollutant concentrations in the Po Valley. Specifically, on November
470 17th, 2023, the Foehn wind was identified by the decrease in relative humidity, the daytime median temperature of 17.2°C
471 (above the daily monthly average of 11.8°C), and the smooth radiation trend, indicating the absence of cloud cover. The air
472 mass trajectory also confirmed the presence of this wind pattern. The increase in SO₂, the source of which still needs to be
473 confirmed, may have further enhanced the formation of new particles, together with the decrease in CS.



474 Similar cases have been observed during the campaign but a detailed classification of Foehn wind event days would be
475 needed to further characterize them in relation to NPF. This case study is consistent with the earlier observations that Foehn
476 wind can create favorable conditions to NPF in Po Valley (Rodríguez et al., 2005) and that it is a significant source of UFP
477 even in urban Milan.



478

479 **Figure 15: a)** NO_x air mass exposure, sulfuric acid (SA) concentration proxy, CS, BLH, BC and SO₂ concentrations, wind speed,
480 relative humidity, temperature, and radiation time series and particle number size distribution surface plot during November 17th,
481 2023. **b)** Source-Receptor Relationship (SRR) for all the trajectories arriving during November 17th, 2023.

482 4 Conclusions

483 This study examines NPF in Milan over one year, revealing that NPF was more intense during spring and summer, resulting
484 in higher concentrations of sub-10 nm particles. In contrast, winter saw higher levels of particles larger than 50 nm, mostly
485 due to the reduced BLH and increased emissions from heating sources. Traffic-related peaks during rush hours were more
486 evident in winter and autumn, but they diminished in spring and summer as atmospheric mixing increased. Our analysis
487 shows that cleaner, well-mixed conditions, particularly with strong northwesterly winds, enhanced NPF by reducing the CS,
488 possibly allowing precursor vapors to participate in the formation of new particles. Reduced air mass exposure to
489 anthropogenic sources and shorter residence time in the Po Valley further supported stronger NPF.



490 The driving mechanisms of NPF vary by location and environmental conditions. Similar patterns have been observed in
491 other urban areas, such as Beijing, China, where Guo et al. (2014) found a higher frequency of NPF events during cleaner
492 periods characterized by lower particle concentrations. During these periods, the reduced CS allowed nucleating vapors to
493 accumulate, facilitating NPF. Conversely, in polluted conditions with high aerosol loading, NPF was suppressed due to the
494 high CS and the abundant pre-existing particles, which provided surfaces that scavenge vapors, inhibiting the NPF process.
495 Also, in Beijing, the occurrence of both clean and polluted periods depended on the meteorology as strong winds descending
496 from the mountains in the north contributed to the cleaning of the atmosphere, while the slower winds from the south
497 favored the accumulation of pollutants (Guo et al., 2014). Our findings suggest that a similar mechanism may be happening
498 in Milan. While the absence of direct precursor vapor measurements precludes us from entirely dismissing the influence of
499 transported chemical precursors, the geographical and environmental context of Milan supports a more plausible
500 explanation. Located in a heavily industrialized, densely populated region with significant agricultural activities, it is
501 reasonable to believe that the reduction of the CS played a more prominent role in initiating NPF, rather than an eventual
502 influx of precursors from the Alps.

503 The relationship between wind speed and NPF is not uniform across all urban sites. For instance, Pushpawela et al. (2019)
504 explored this relationship in Brisbane, Australia, and observed that NPF was more likely to happen on days with lower wind
505 speed, a finding opposite to that in Milan and other highly polluted environments. Their comparative analysis suggested that
506 the impact of wind speed on NPF depends on the level of pollution and the distribution of precursor vapors. In relatively
507 cleaner urban areas like Brisbane, where the accumulation of precursors can enhance NPF, a lower wind speed facilitates this
508 process. In contrast, in highly polluted cities like Beijing, a low wind speed increases the CS, suppressing NPF. At higher
509 wind speed, the reduction in CS can promote NPF in polluted areas by clearing pre-existing particles, whereas in cleaner
510 cities, the removal of precursor vapors can inhibit NPF. Our study locates Milan within this framework as a highly polluted
511 city where the interplay between wind speed, CS, and precursor vapor concentrations played a critical role in the NPF
512 dynamics.

513

514 The findings hint at potential implications for air quality in Milan. Long-term reductions in PM_{10} and $PM_{2.5}$ concentrations,
515 potentially driven by regulatory measures, could lead to stronger NPF, increasing the concentrations of UFP. This highlights
516 the need for detailed studies on precursor vapors and on the chemical pathways leading to NPF to fully understand their role
517 in the NPF process, especially in relation to low CS episodes. Future research should focus on the direct measurements of
518 these precursors to clarify their contributions, whether local or transported. Comparative studies in other polluted urban
519 environments are also crucial to understand regional differences in NPF dynamics. Long-term monitoring of aerosol
520 concentrations at all size ranges and NPF events, in relation to urban development and pollution control, would provide
521 valuable insights into the effectiveness and results of air quality strategies.



522 **Data availability**

523 The raw data are available from the corresponding author (myriam.agro@helsinki.fi) upon request.

524 **Author contribution**

525 The study was designed by FB and TP. MA, SM, IG, PF, AB, CO, AB, JS participated in the installation and the operation
526 of the instruments. MA analysed the data. MB and GC performed the modelling simulations and analysis. MA prepared the
527 manuscript. All the coauthors contributed to the discussion and interpretation of the results and the revision of the article.

528 **Competing interests**

529 Some authors are members of the editorial board of journal Atmospheric Chemistry and Physics.

530 **Acknowledgments**

531 We acknowledge the use of the Matlab package psm-dataflow-tools by Lauri Ahonen for the PSM inversion. We thank the
532 Department of Direzione tecnica monitoraggi e prevenzione del rischio naturale of Regional Agency for Environmental
533 Protection of Lombardy for providing the boundary layer height data. Model simulations were performed on the Mahti
534 supercomputer of the Finnish IT Center for Science (CSC).

535 **Financial support**

536 This project received funding from the European Union's Horizon 2020 research and innovation programme under grant
537 agreement No 101036245 (RI-URBANS).

538 We thank the ACCC Flagship, funded by the Academy of Finland grant numbers 337549 (UH) and 337552 (FMI).

539 **References**

540 Aliaga, D., Tuovinen, S., Zhang, T., Lampilahti, J., Li, X., Ahonen, L., Kokkonen, T., Nieminen, T., Hakala, S., Paasonen,
541 P., Bianchi, F., Worsnop, D., Kerminen, V.-M., and Kulmala, M.: Nanoparticle ranking analysis: determining new particle
542 formation (NPF) event occurrence and intensity based on the concentration spectrum of formed (sub-5 nm) particles,
543 *Aerosol Res.*, 1, 81–92, <https://doi.org/10.5194/ar-1-81-2023>, 2023.

544 Bae, M.-S., Schwab, J. J., Hogrefe, O., Frank, B. P., Lala, G. G., and Demerjian, K. L.: Characteristics of size distributions at
545 urban and rural locations in New York, *Atmospheric Chem. Phys.*, 10, 4521–4535, <https://doi.org/10.5194/acp-10-4521-2010>, 2010.



- 547 548 Batchvarova, E. and Gryning, S.-E.: Applied model for the growth of the daytime mixed layer, *Bound.-Layer Meteorol.*, 56, 261–274, <https://doi.org/10.1007/BF00120423>, 1991.
- 549 550 551 552 Bousiotis, D., Pope, F. D., Beddows, D. C. S., Dall’Osto, M., Massling, A., Nøjgaard, J. K., Nordstrøm, C., Niemi, J. V., Portin, H., Petäjä, T., Perez, N., Alastuey, A., Querol, X., Kouvarakis, G., Mihalopoulos, N., Vratolis, S., Eleftheriadis, K., Wiedensohler, A., Weinhold, K., Merkel, M., Tuch, T., and Harrison, R. M.: A phenomenology of new particle formation (NPF) at 13 European sites, *Atmospheric Chem. Phys.*, 21, 11905–11925, <https://doi.org/10.5194/acp-21-11905-2021>, 2021.
- 553 554 555 Brean, J., Beddows, D. C. S., Shi, Z., Temime-Roussel, B., Marchand, N., Querol, X., Alastuey, A., Minguillón, M. C., and Harrison, R. M.: Molecular insights into new particle formation in Barcelona, Spain, *Atmospheric Chem. Phys.*, 20, 10029–10045, <https://doi.org/10.5194/acp-20-10029-2020>, 2020.
- 556 557 558 Brioude, J., Arnold, D., Stohl, A., Cassiani, M., Morton, D., Seibert, P., Angevine, W., Evan, S., Dingwell, A., Fast, J. D., Easter, R. C., Pisso, I., Burkhardt, J., and Wotawa, G.: The Lagrangian particle dispersion model FLEXPART-WRF version 3.1, *Geosci. Model Dev.*, 6, 1889–1904, <https://doi.org/10.5194/gmd-6-1889-2013>, 2013.
- 559 560 561 562 563 Cai, J., Sulo, J., Gu, Y., Holm, S., Cai, R., Thomas, S., Neuberger, A., Mattsson, F., Paglione, M., Decesari, S., Rinaldi, M., Yin, R., Aliaga, D., Huang, W., Li, Y., Gramlich, Y., Ciarelli, G., Quéléver, L., Sarnela, N., Lehtipalo, K., Zannoni, N., Wu, C., Nie, W., Kangasluoma, J., Mohr, C., Kulmala, M., Zha, Q., Stolzenburg, D., and Bianchi, F.: Elucidating the mechanisms of atmospheric new particle formation in the highly polluted Po Valley, Italy, *Atmospheric Chem. Phys.*, 24, 2423–2441, <https://doi.org/10.5194/acp-24-2423-2024>, 2024.
- 564 565 Chen, F. and Dudhia, J.: Coupling an Advanced Land Surface–Hydrology Model with the Penn State–NCAR MM5 Modeling System. Part I: Model Implementation and Sensitivity, 2001.
- 566 567 568 569 570 Dada, L., Ylivinkka, I., Baalbaki, R., Li, C., Guo, Y., Yan, C., Yao, L., Sarnela, N., Jokinen, T., Daellenbach, K. R., Yin, R., Deng, C., Chu, B., Nieminen, T., Wang, Y., Lin, Z., Thakur, R. C., Kontkanen, J., Stolzenburg, D., Sipilä, M., Hussein, T., Paasonen, P., Bianchi, F., Salma, I., Weidinger, T., Pikridas, M., Sciare, J., Jiang, J., Liu, Y., Petäjä, T., Kerminen, V.-M., and Kulmala, M.: Sources and sinks driving sulfuric acid concentrations in contrasting environments: implications on proxy calculations, *Atmospheric Chem. Phys.*, 20, 11747–11766, <https://doi.org/10.5194/acp-20-11747-2020>, 2020.
- 571 572 573 574 Dada, L., Okuljar, M., Shen, J., Olin, M., Wu, Y., Heimsch, L., Herlin, I., Kankaanrinta, S., Lampimäki, M., Kalliokoski, J., Baalbaki, R., Lohila, A., Petäjä, T., Maso, M. D., Duplissy, J., Kerminen, V.-M., and Kulmala, M.: The synergistic role of sulfuric acid, ammonia and organics in particle formation over an agricultural land, *Environ. Sci. Atmospheres*, 3, 1195–1211, <https://doi.org/10.1039/D3EA00065F>, 2023.
- 575 576 577 Dai, L., Zhao, Y., Zhang, L., Chen, D., and Wu, R.: Particle number size distributions and formation and growth rates of different new particle formation types of a megacity in China, *J. Environ. Sci.*, 131, 11–25, <https://doi.org/10.1016/j.jes.2022.07.029>, 2023.
- 578 579 580 Dal Maso, M., Kulmala, M., Riipinen, I., Wagner, R., Hussein, T., Aalto, P. P., and Lehtinen, K. E. J.: Formation and growth of fresh atmospheric aerosols: eight years of aerosol size distribution data from SMEAR II, Hyytiälä, Finland, *Boreal Environ. Res.*, 10, 323–336, <https://doi.org/10.60910/yq6q-vj10>, 2005.
- 581 582 Fuchs, N. A. and Sutugin, A. G.: HIGH-DISPersed AEROSOLS, in: *Topics in Current Aerosol Research*, edited by: Hidy, G. M. and Brock, J. R., Pergamon, 1, <https://doi.org/10.1016/B978-0-08-016674-2.50006-6>, 1971.
- 583 584 585 Gordon, H., Kirkby, J., Baltensperger, U., Bianchi, F., Breitenlechner, M., Curtius, J., Dias, A., Dommen, J., Donahue, N. M., Dunne, E. M., Duplissy, J., Ehrhart, S., Flagan, R. C., Frege, C., Fuchs, C., Hansel, A., Hoyle, C. R., Kulmala, M., Kurten, A., Lehtipalo, K., Makhmudov, V., Molteni, U., Rissanen, M. P., Stozkhov, Y., Trostl, J., Tsagkogeorgas, G.,



- 586 Wagner, R., Williamson, C., Wimmer, D., Winkler, P. M., Yan, C., and Carslaw, K. S.: Causes and importance of new
587 particle formation in the present-day and preindustrial atmospheres, *J. Geophys. Res. Atmospheres*, 122, 8739–8760,
588 <https://doi.org/10.1002/2017JD026844>, 2017.
- 589 Gormley, P. G. and Kennedy, M.: Diffusion from a Stream Flowing through a Cylindrical Tube, *Proc. R. Ir. Acad. Sect.*
590 *Math. Phys. Sci.*, 52, 163–169, 1948.
- 591 Guo, S., Hu, M., Zamora, M. L., Peng, J., Shang, D., Zheng, J., Du, Z., Wu, Z., Shao, M., Zeng, L., Molina, M. J., and
592 Zhang, R.: Elucidating severe urban haze formation in China, *Proc. Natl. Acad. Sci.*, 111, 17373–17378,
593 <https://doi.org/10.1073/pnas.1419604111>, 2014.
- 594 Hakala, S., Vakkari, V., Bianchi, F., Dada, L., Deng, C., Dännenbach, K. R., Fu, Y., Jiang, J., Kangasluoma, J., Kujansuu, J.,
595 Liu, Y., Petäjä, T., Wang, L., Yan, C., Kulmala, M., and Paasonen, P.: Observed coupling between air mass history,
596 secondary growth of nucleation mode particles and aerosol pollution levels in Beijing, *Environ. Sci. Atmospheres*, 2, 146–
597 164, <https://doi.org/10.1039/D1EA00089F>, 2022.
- 598 Hamed, A., Joutsensaari, J., Mikkonen, S., Sogacheva, L., Dal Maso, M., Kulmala, M., Cavalli, F., Fuzzi, S., Facchini, M.
599 C., Decesari, S., Mircea, M., Lehtinen, K. E. J., and Laaksonen, A.: Nucleation and growth of new particles in Po Valley,
600 Italy, *Atmospheric Chem. Phys.*, 7, 355–376, <https://doi.org/10.5194/acp-7-355-2007>, 2007.
- 601 Hong, S.-Y., Dadhia, J., and Chen, S.-H.: A Revised Approach to Ice Microphysical Processes for the Bulk Parameterization
602 of Clouds and Precipitation, 2004.
- 603 Kerminen, V.-M., Chen, X., Vakkari, V., Petäjä, T., Kulmala, M., and Bianchi, F.: Atmospheric new particle formation and
604 growth: review of field observations, *Environ. Res. Lett.*, 13, 103003, <https://doi.org/10.1088/1748-9326/aadf3c>, 2018.
- 605 Kontkanen, J., Järvinen, E., Manninen, H. E., Lehtipalo, K., Kangasluoma, J., Decesari, S., Gobbi, G. P., Laaksonen, A.,
606 Petäjä, T., and Kulmala, M.: High concentrations of sub-3nm clusters and frequent new particle formation observed in the Po
607 Valley, Italy, during the PEGASOS 2012 campaign, *Atmospheric Chem. Phys.*, 16, 1919–1935, <https://doi.org/10.5194/acp-16-1919-2016>, 2016.
- 609 Kuenen, J., Dellaert, S., Visschedijk, A., Jalkanen, J.-P., Super, I., and Denier van der Gon, H.: CAMS-REG-v4: a state-of-
610 the-art high-resolution European emission inventory for air quality modelling, *Earth Syst. Sci. Data*, 14, 491–515,
611 <https://doi.org/10.5194/essd-14-491-2022>, 2022.
- 612 Kulmala, M., Petäjä, T., Nieminen, T., Sipilä, M., Manninen, H. E., Lehtipalo, K., Dal Maso, M., Aalto, P. P., Junninen, H.,
613 Paasonen, P., Riipinen, I., Lehtinen, K. E. J., Laaksonen, A., and Kerminen, V.-M.: Measurement of the nucleation of
614 atmospheric aerosol particles, *Nat. Protoc.*, 7, 1651–1667, <https://doi.org/10.1038/nprot.2012.091>, 2012.
- 615 Kulmala, M., Kontkanen, J., Junninen, H., Lehtipalo, K., Manninen, H. E., Nieminen, T., Petäjä, T., Sipilä, M.,
616 Schobesberger, S., Rantala, P., Franchin, A., Jokinen, T., Järvinen, E., Äijälä, M., Kangasluoma, J., Hakala, J., Aalto, P. P.,
617 Paasonen, P., Mikkilä, J., Vanhanen, J., Aalto, J., Hakola, H., Makkonen, U., Ruuskanen, T., Mauldin, R. L., Duplissy, J.,
618 Vehkamäki, H., Bäck, J., Kortelainen, A., Riipinen, I., Kurtén, T., Johnston, M. V., Smith, J. N., Ehn, M., Mentel, T. F.,
619 Lehtinen, K. E. J., Laaksonen, A., Kerminen, V.-M., and Worsnop, D. R.: Direct observations of atmospheric aerosol
620 nucleation, *Science*, 339, 943–946, <https://doi.org/10.1126/science.1227385>, 2013.
- 621 Kulmala, M., Dada, L., Daellenbach, K. R., Yan, C., Stolzenburg, D., Kontkanen, J., Ezhova, E., Hakala, S., Tuovinen, S.,
622 Kokkonen, T. V., Kurppa, M., Cai, R., Zhou, Y., Yin, R., Baalbaki, R., Chan, T., Chu, B., Deng, C., Fu, Y., Ge, M., He, H.,
623 Heikkilä, L., Junninen, H., Liu, Y., Lu, Y., Nie, W., Rusanen, A., Vakkari, V., Wang, Y., Yang, G., Yao, L., Zheng, J.,
624 Kujansuu, J., Kangasluoma, J., Petäjä, T., Paasonen, P., Järvi, L., Worsnop, D., Ding, A., Liu, Y., Wang, L., Jiang, J.,



- 625 626 Bianchi, F., and Kerminen, V.-M.: Is reducing new particle formation a plausible solution to mitigate particulate air pollution
in Beijing and other Chinese megacities?, *Faraday Discuss.*, 226, 334–347, <https://doi.org/10.1039/D0FD00078G>, 2021.
- 627 628 629 Kulmala, M., Junninen, H., Dada, L., Salma, I., Weidinger, T., Thén, W., Vörösmarty, M., Komsaare, K., Stolzenburg, D.,
Cai, R., Yan, C., Li, X., Deng, C., Jiang, J., Petäjä, T., Nieminen, T., and Kerminen, V.-M.: Quiet New Particle Formation in
the Atmosphere, *Front. Environ. Sci.*, 10, 912385, <https://doi.org/10.3389/fenvs.2022.912385>, 2022.
- 630 631 632 Lampimäki, M., Baalbaki, R., Ahonen, L., Korhonen, F., Cai, R., Chan, T., Stolzenburg, D., Petäjä, T., Kangasluoma, J.,
Vanhainen, J., and Lehtipalo, K.: Novel aerosol diluter – Size dependent characterization down to 1 nm particle size, *J. Aerosol Sci.*, 172, 106180, <https://doi.org/10.1016/j.jaerosci.2023.106180>, 2023.
- 633 634 635 636 Lehtipalo, K., Ahonen, L. R., Baalbaki, R., Sulo, J., Chan, T., Laurila, T., Dada, L., Duplissy, J., Miettinen, E., Vanhanen, J.,
Kangasluoma, J., Kulmala, M., Petäjä, T., and Jokinen, T.: The standard operating procedure for Airmodus Particle Size
Magnifier and nano-Condensation Nucleus Counter, *J. Aerosol Sci.*, 159, 105896,
<https://doi.org/10.1016/j.jaerosci.2021.105896>, 2022.
- 637 638 639 Manninen, H. E., Mirme, S., Mirme, A., Petäjä, T., and Kulmala, M.: How to reliably detect molecular clusters and
nucleation mode particles with Neutral cluster and Air Ion Spectrometer (NAIS), *Atmospheric Meas. Tech.*, 9, 3577–3605,
<https://doi.org/10.5194/amt-9-3577-2016>, 2016.
- 640 641 Merikanto, J., Spracklen, D. V., Mann, G. W., Pickering, S. J., and Carslaw, K. S.: Impact of nucleation on global CCN,
Atmospheric Chem. Phys., 9, 8601–8616, <https://doi.org/10.5194/acp-9-8601-2009>, 2009.
- 642 643 644 Mirme, S. and Mirme, A.: The mathematical principles and design of the NAIS – a spectrometer for the measurement of
cluster ion and nanometer aerosol size distributions, *Atmospheric Meas. Tech.*, 6, 1061–1071, <https://doi.org/10.5194/amt-6-1061-2013>, 2013.
- 645 646 647 Mlawer, E. J., Taubman, S. J., Brown, P. D., Iacono, M. J., and Clough, S. A.: Radiative transfer for inhomogeneous
atmospheres: RRTM, a validated correlated-k model for the longwave, *J. Geophys. Res. Atmospheres*, 102, 16663–16682,
<https://doi.org/10.1029/97JD00237>, 1997.
- 648 649 650 651 652 653 654 Nieminen, T., Kerminen, V.-M., Petäjä, T., Aalto, P. P., Arshinov, M., Asmi, E., Baltensperger, U., Beddows, D. C. S.,
Beukes, J. P., Collins, D., Ding, A., Harrison, R. M., Henzing, B., Hooda, R., Hu, M., Hörrak, U., Kivekäs, N., Komsaare,
K., Krejci, R., Kristensson, A., Laakso, L., Laaksonen, A., Leaitch, W. R., Lihavainen, H., Mihalopoulos, N., Németh, Z.,
Nie, W., O'Dowd, C., Salma, I., Sellegri, K., Svensson, B., Swietlicki, E., Tunved, P., Ulevicius, V., Vakkari, V., Vana,
M., Wiedensohler, A., Wu, Z., Virtanen, A., and Kulmala, M.: Global analysis of continental boundary layer new particle
formation based on long-term measurements, *Atmospheric Chem. Phys.*, 18, 14737–14756, <https://doi.org/10.5194/acp-18-14737-2018>, 2018.
- 655 656 Pushpawela, B., Jayaratne, R., and Morawska, L.: The influence of wind speed on new particle formation events in an urban
environment, *Atmospheric Res.*, 215, 37–41, <https://doi.org/10.1016/j.atmosres.2018.08.023>, 2019.
- 657 658 659 Rodríguez, S., Van Dingenen, R., Putaud, J.-P., Martins-Dos Santos, S., and Roselli, D.: Nucleation and growth of new
particles in the rural atmosphere of Northern Italy—relationship to air quality monitoring, *Atmos. Environ.*, 39, 6734–6746,
<https://doi.org/10.1016/j.atmosenv.2005.07.036>, 2005.
- 660 661 662 663 Rönkkö, T., Kuuluvainen, H., Karjalainen, P., Keskinen, J., Hillamo, R., Niemi, J. V., Pirjola, L., Timonen, H. J., Saarikoski, I.,
Saukko, E., Järvinen, A., Silvennoinen, H., Rostedt, A., Olin, M., Yli-Ojanperä, J., Nousiainen, P., Kousa, A., and Dal
Maso, M.: Traffic is a major source of atmospheric nanocluster aerosol, *Proc. Natl. Acad. Sci.*, 114, 7549–7554,
<https://doi.org/10.1073/pnas.1700830114>, 2017.



- 664 Salma, I., Borsós, T., Weidinger, T., Aalto, P., Hussein, T., Dal Maso, M., and Kulmala, M.: Production, growth and
665 properties of ultrafine atmospheric aerosol particles in an urban environment, *Atmospheric Chem. Phys.*, 11, 1339–1353,
666 <https://doi.org/10.5194/acp-11-1339-2011>, 2011.
- 667 Schraufnagel, D. E.: The health effects of ultrafine particles, *Exp. Mol. Med.*, 52, 311–317, <https://doi.org/10.1038/s12276-020-0403-3>, 2020.
- 669 Seinfeld, J. H. and Pandis, S. N.: *Atmospheric Chemistry and Physics: From Air Pollution to Climate Change*, John Wiley &
670 Sons, 1146 pp., 2016.
- 671 Simpson, D., Benedictow, A., Berge, H., Bergström, R., Emberson, L. D., Fagerli, H., Flechard, C. R., Hayman, G. D.,
672 Gauss, M., Jonson, J. E., Jenkin, M. E., Nyíri, A., Richter, C., Semeena, V. S., Tsyro, S., Tuovinen, J.-P., Valdebenito, Á.,
673 and Wind, P.: The EMEP MSC-W chemical transport model – technical description, *Atmospheric Chem. Phys.*, 12,
674 7825–7865, <https://doi.org/10.5194/acp-12-7825-2012>, 2012.
- 675 Spracklen, D. V., Carslaw, K. S., Kulmala, M., Kerminen, V.-M., Sihto, S.-L., Riipinen, I., Merikanto, J., Mann, G. W.,
676 Chipperfield, M. P., Wiedensohler, A., Birmili, W., and Lihavainen, H.: Contribution of particle formation to global cloud
677 condensation nuclei concentrations, *Geophys. Res. Lett.*, 35, <https://doi.org/10.1029/2007GL033038>, 2008.
- 678 Trechera, P., Garcia-Marlès, M., Liu, X., Reche, C., Pérez, N., Savadkoohi, M., Beddows, D., Salma, I., Vörösmarty, M.,
679 Casans, A., Casquero-Vera, J. A., Hueglin, C., Marchand, N., Chazeau, B., Gille, G., Kalkavouras, P., Mihalopoulos, N.,
680 Ondracek, J., Zikova, N., Niemi, J. V., Manninen, H. E., Green, D. C., Tremper, A. H., Norman, M., Vratolis, S.,
681 Eleftheriadis, K., Gómez-Moreno, F. J., Alonso-Blanco, E., Gerwig, H., Wiedensohler, A., Weinhold, K., Merkel, M.,
682 Bastian, S., Petit, J.-E., Favez, O., Crumeyrolle, S., Ferlay, N., Martins Dos Santos, S., Putaud, J.-P., Timonen, H.,
683 Lampilahti, J., Asbach, C., Wolf, C., Kaminski, H., Altug, H., Hoffmann, B., Rich, D. Q., Pandolfi, M., Harrison, R. M.,
684 Hopke, P. K., Petäjä, T., Alastuey, A., and Querol, X.: Phenomenology of ultrafine particle concentrations and size
685 distribution across urban Europe, *Environ. Int.*, 172, 107744, <https://doi.org/10.1016/j.envint.2023.107744>, 2023.
- 686 Vallabani, N. V. S., Gruzieva, O., Elihn, K., Juárez-Facio, A. T., Steimer, S. S., Kuhn, J., Silvergren, S., Portugal, J., Piña,
687 B., Olofsson, U., Johansson, C., and Karlsson, H. L.: Toxicity and health effects of ultrafine particles: Towards an
688 understanding of the relative impacts of different transport modes, *Environ. Res.*, 231, 116186,
689 <https://doi.org/10.1016/j.envres.2023.116186>, 2023.
- 690 Vecchi, R., Marcazzan, G., Valli, G., Ceriani, M., and Antoniazzi, C.: The role of atmospheric dispersion in the seasonal
691 variation of PM1 and PM2.5 concentration and composition in the urban area of Milan (Italy), *Atmos. Environ.*, 38, 4437–
692 4446, <https://doi.org/10.1016/j.atmosenv.2004.05.029>, 2004.
- 693 Wagner, R., Manninen, H. E., Franchin, A., Lehtipalo, K., Mirme, S., Steiner, G., Petäjä, T., and Kulmala, M.: On the
694 accuracy of ion measurements using a Neutral cluster and Air Ion Spectrometer, *Boreal Environ. Res.*, 21, (3-4), 230-241,
695 <http://hdl.handle.net/10138/165313>, 2016.
- 696 Wang, S. C. and Flagan, R. C.: Scanning Electrical Mobility Spectrometer, *Aerosol Sci. Technol.*, 13, 230–240,
697 <https://doi.org/10.1080/02786829008959441>, 1990.
- 698 Wolfram Research, Inc.: *Mathematica*, Version 14.1, Champaign, IL, USA, 2025.
- 699 Yao, L., Garmash, O., Bianchi, F., Zheng, J., Yan, C., Kontkanen, J., Junninen, H., Mazon, S. B., Ehn, M., Paasonen, P.,
700 Sipilä, M., Wang, M., Wang, X., Xiao, S., Chen, H., Lu, Y., Zhang, B., Wang, D., Fu, Q., Geng, F., Li, L., Wang, H., Qiao,
701 L., Yang, X., Chen, J., Kerminen, V.-M., Petäjä, T., Worsnop, D. R., Kulmala, M., and Wang, L.: Atmospheric new particle



702 formation from sulfuric acid and amines in a Chinese megacity, *Science*, 361, 278–281,
703 <https://doi.org/10.1126/science.aa04839>, 2018.

704 Zhao, B., Donahue, N. M., Zhang, K., Mao, L., Shrivastava, M., Ma, P.-L., Shen, J., Wang, S., Sun, J., Gordon, H., Tang, S.,
705 Fast, J., Wang, M., Gao, Y., Yan, C., Singh, B., Li, Z., Huang, L., Lou, S., Lin, G., Wang, H., Jiang, J., Ding, A., Nie, W.,
706 Qi, X., Chi, X., and Wang, L.: Global variability in atmospheric new particle formation mechanisms, *Nature*, 631, 98–105,
707 <https://doi.org/10.1038/s41586-024-07547-1>, 2024.

708 Zilitinkevich, S. and Baklanov, A.: Calculation Of The Height Of The Stable Boundary Layer In Practical Applications,
709 *Bound.-Layer Meteorol.*, 105, 389–409, <https://doi.org/10.1023/A:1020376832738>, 2002.

710